Journal of Astronomical Telescopes, Instruments, and Systems

AstronomicalTelescopes.SPIEDigitalLibrary.org

Polarization modeling and predictions for Daniel K. Inouye Solar Telescope part 1: telescope and example instrument configurations

David M. Harrington
Stacey R. Sueoka

SPIE.

David M. Harrington, Stacey R. Sueoka, "Polarization modeling and predictions for Daniel K. Inouye Solar Telescope part 1: telescope and example instrument configurations," *J. Astron. Telesc. Instrum. Syst.* **3**(1), 018002 (2017), doi: 10.1117/1.JATIS.3.1.018002.

Polarization modeling and predictions for Daniel K. Inouye Solar Telescope part 1: telescope and example instrument configurations

David M. Harrington[a,*] and Stacey R. Sueoka[b]
[a]National Solar Observatory, Hawaii, United States
[b]National Solar Observatory, Boulder, Colorado, United States

Abstract. We outline polarization performance calculations and predictions for the Daniel K. Inouye Solar Telescope (DKIST) optics and show Mueller matrices for two of the first light instruments. Telescope polarization is due to polarization-dependent mirror reflectivity and rotations between groups of mirrors as the telescope moves in altitude and azimuth. The Zemax optical modeling software has polarization ray-trace capabilities and predicts system performance given a coating prescription. We develop a model coating formula that approximates measured witness sample polarization properties. Estimates show the DKIST telescope Mueller matrix as functions of wavelength, azimuth, elevation, and field angle for the cryogenic near infra-red spectro-polarimeter (CryoNIRSP) and visible spectro-polarimeter. Footprint variation is substantial and shows vignetted field points will have strong polarization effects. We estimate 2% variation of some Mueller matrix elements over the 5-arc min CryoNIRSP field. We validate the Zemax model by showing limiting cases for flat mirrors in collimated and powered designs that compare well with theoretical approximations and are testable with lab ellipsometers.
 [DOI: 10.1117/1.JATIS.3.1.018002]

Keywords: instrumentation; polarization; Mueller matrix; Daniel K. Inouye Solar Telescope; cryogenic near infra-red spectro-polarimeter; visible spectro-polarimeter.

Paper 16039P received Jul. 13, 2016; accepted for publication Jan. 9, 2017; published online Feb. 7, 2017.

1 Predicting DKIST Polarization

Predicting the Mueller matrix of a many mirror system with highly powered optics across the field of view (FoV) is an important tool for the design and use of large astronomical telescopes. The Daniel K. Inouye Solar Telescope (DKIST) on Haleakalā, Maui, Hawai'i has a 4.2-m off-axis $f/2$ primary mirror (4.0 m illuminated) and a suite of polarimetric instrumentation in a coudé laboratory.[1–3] The telescope uses seven mirrors to feed light to the coudé lab.[1,4–8] Operations involve four polarimetric instruments presently spanning the 380- to 5000-nm wavelength range. A train of dichroic beam splitters allows for rapid changing of instrument configurations and simultaneous operation of three polarimetric instruments covering 380 to 1800 nm.[7–10] Complex modulation and calibration strategies are required for such a mulitinstrument system.[7,8,11–14] The planned 4-m European Solar Telescope (EST), though on-axis, will also require similar calibration considerations.[15–18] Many solar and night-time telescopes are calibrating complex optical pathways.[19–42]

Several other large astronomical telescopes are in development and include plans for polarimeters. For many years, a night-time spectropolarimeter on the 4-m Advanced Electro-Optical System (AEOS) Telescope on Maui has been pursuing a campaign of polarization calibration.[43–47] We have developed Zemax modeling tools to compute the polarization of an optical system provided the optical model and the coating prescription for the optics. These Zemax modeling tools have been used on the AEOS telescope and the HiVIS spectropolarimeter. We also apply the tools here to the DKIST telescope and a predict Mueller matrices for two of the first light polarimetric instruments. We refer the reader to recent papers outlining the various capabilities of the first-light instruments.[1,3,7,8]

In this work, we follow standard notation. The Stokes vector is denoted as $\mathbf{S} = [I, Q, U, V]^{\mathrm{T}}$. The Mueller matrix is the 4×4 matrix that transfers Stokes vectors. Each element of the Mueller matrix is denoted as the transfer coefficient.[48–50] For instance, the coefficient (1,0) in the first row transfers Q to I and is denoted QI. The first row is denoted II, QI, UI, VI. The first column of the Mueller matrix is thus II, IQ, IU, IV.

1.1 *DKIST Optics Overview*

The DKIST optical train includes an off-axis 4-m diameter parabolic primary mirror (M1) that creates an $f/2$ prime focus. At prime focus, there is a heat stop, which limits the FoV to roughly 5-arc min and reduces the heat load on all downstream optics. The secondary mirror (M2) is also an off-axis ellipse (conic −0.54), which relays this beam to an $f/13$ Gregorian focus. Just above the Gregorian focus, there is an optical station for insertion and removal of several masks, targets, artificial light sources, and a set of polarization calibration optics. There are also field stops for 2.8-arc min diameter and 5-arc min diameter at Gregorian focus. The third mirror (M3) is a flat fold mirror at 45-deg incidence angle that directs the light toward the off-axis ellipse (M4, conic −0.37). This parabolic mirror changes the diverging $f/13$ beam to a converging $f/53$ beam and creates

*Address all correspondence to: David M. Harrington, E-mail: harrington@nso.edu

a pupil conjugate plane near the next flat steering mirror (M5). Between M4 and M5 is also the elevation axis of rotation for the telescope. M5 folds at 30 deg and also functions as a fast steering mirror with tip/tilt capability. The sixth mirror in the system (M6) is also a flat and directs the beam vertically downward toward the coudé lab folding at a 60-deg angle. The seventh mirror is another flat fold mirror that levels the beam into the coudé laboratory folding at 90-deg incidence angle. The eighth mirror (M8) is an off-axis parabola that collimates the beam. The ninth mirror is a flat fold that directs the beam toward the deformable mirror (DM) as part of the integrated adaptive optics system. The pupil of the system is conjugated near the flat DM and this represents the 10th optic in the system (M10).

Figure 1 shows the optical concept for the system. There are four powered optics that perform the relays. In order, the beam has an $f/2$ prime focus, an $f/13$ Gregorian focus, an $f/53$ intermediate focus, and a collimated coudé laboratory.

The coudé lab was designed to allow simultaneous operation of many instruments observing different wavelengths by using several custom dichroic beam splitters. An adaptive optics system was also integrated into the design. The wave front sensor (WFS) of the adaptive optics system is fed by a reflection off the uncoated front surface of a window, denoted WFS-BS1 that is mounted after the DM. There are three polarimetric instruments that use the adaptive optics system: the visible spectro-polarimeter (ViSP), the visible tunable filter (VTF), and the diffraction limited near-infrared spectro-polarimeter (DL-NIRSP). In addition to these polarimetric instruments, there are two arms of a high-resolution imaging system that also use the AO feed. The visible broadband imager (VBI) is essentially two separate instruments, one a red imager (VBI-red) and the other a blue imager (VBI-blue).

Another first light instrument was designed to include infrared capabilities at wavelengths as long as 5000 nm and was optimized for seeing-limited science cases. This instrument, the cryogenic near-infrared spectro-polarimeter (CryoNIRSP) does not use the adaptive optics system and has a separate optical path after M9. For CryoNIRSP, an additional fold mirror (M9a) is inserted into the beam after M9 to direct light to the system feed optics.

For calibration purposes, we will describe a possible configuration using the AO system and the several simultaneous channels of the various instruments. Note that both ViSP and DL-NIRSP have three separate cameras that can record three separately configured wavelengths each. Many configurations are possible and the spectrographs are designed to be reconfigurable in minutes with substantial automation. As an example, DL-NIRSP configuration of the three spectrographs could be (789 or 854.2 nm) on camera 1, (1074.7 or 1083 nm) on camera 2, and (1430 or 1565 nm) on camera 3. At the same time, ViSP could be configured to a vast array of possible spectral lines covering 380 to 1100 nm. Depending on how the dichroics are arranged, the various instruments could be sent limited ranges of wavelengths permitting only some of the cameras to be used.

One setup could configure the first two dichroics CL2 and CL2a to send the VBI-blue camera wavelengths shorter than 430 nm, ViSP wavelengths to 660 nm, VTF to 860 nm, and DL-NIRSP the long wavelength bandpass. With this setup, ViSP could be configured to use at least two of the cameras between 430 and 660 nm, and the DL-NIRSP could use two of the three cameras working at wavelengths longer than 1000 nm. We would need to have polarization calibrations for 5 polarimetric channels (2 on ViSP, VTF, 2 on DL-NIRSP) with calibrations done after the dichroics are installed.

Figure 2 shows a conceptual optical schematic along with Zemax and solid models of the system. The telescope is a classical elevation over azimuth design. In addition to the usual azimuth and elevation degrees of freedom, the entire laboratory floor rotates freely. This coudé rotator is one of the major construction components and gives independent optical control of the field rotation without requiring the use of a three-mirror derotator (K cell)[1] or more optics such as THEMIS[51] or the

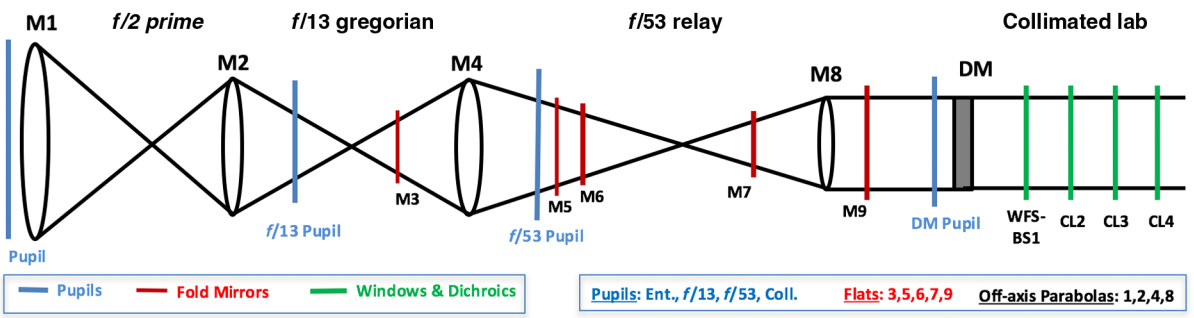

Fig. 1 The DKIST telescope feed optics conceptual design. Only powered optics are shown. All powered optics are off-axis parabolas. The beam has an $f/2$ prime focus, an $f/13$ Gregorian focus, an $f/53$ intermediate focus, and a collimated coudé laboratory where all first-light instruments are installed. All flat mirrors are shown as red lines. Pupil conjugate planes are shown as vertical blue lines. The entrance pupil of this unobscured system is a 4.0-m diameter aperture mask ring mounted above the 4.24-m diameter primary mirror. The DM is shown as a thick gray box. After the DM, there are several beam splitters as part of the coudé laboratory. The WFS of the adaptive optics system is fed by a reflection off the uncoated front surface of a window, denoted WFS-BS1. After this optic, there are several dichroic beam splitters that are interchangeable denoted as CL *N* where *N* is the numeric identifier. These dichroics are designed to be reconfigured to send various wavelength ranges to various instruments. We also note that one of the polarimetric instruments (Cryo-NIRSP) inserts a mirror after M9 and does not use the adaptive optics system.

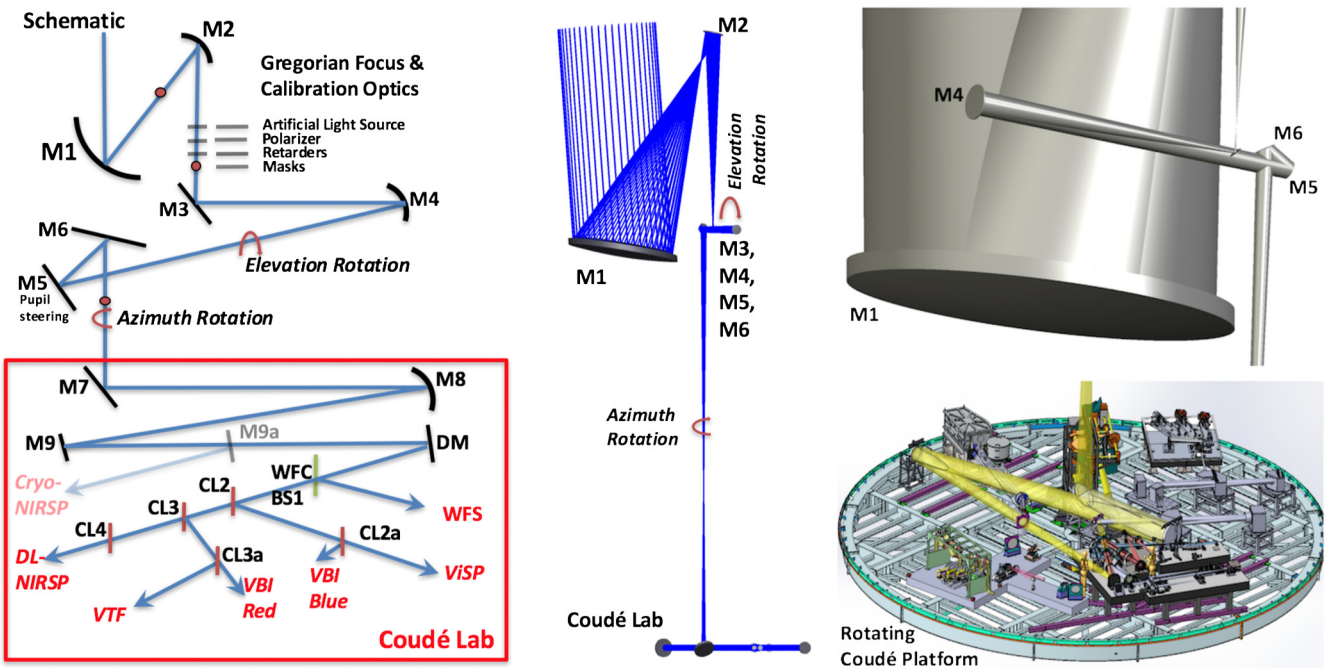

Fig. 2 The DKIST optics design and schematic. The left panel shows a cartoon schematic for the optical path (not to scale, not an actual layout, fold angles, not accurate). The primary and secondary mirrors relay the beam to the $f/13$ Gregorian focus and an optical system where calibration optics can be inserted. The M3–M6 optics assist with the articulation of the telescope, and feed the $f/53$ beam down to the coudé laboratory. The beam is then leveled and collimated into the adaptive optics system by M7–M10. The optional insertion of a flat mirror to bypass the adaptive optics and feed the CryoNIRSP instrument is also shown. The wave-front sensor beam splitter (WFS-BS1) and all the dichroic beam splitters (CL *N*) are shown distributing the different wavelengths to all the coudé instruments. The middle panel shows the Zemax design beginning from the beam entering the dome and ending at the DM in the coudé laboratory. Mirrors M3–M6 are packaged in an assembly that allows the telescope structure to rotate in elevation. The top right image shows a solid model of the optical beam highlighting the Gregorian focus and the optics M3–M6. The primary (M1) and the 4-m diameter beam is seen behind optics M3 to M6. The bottom right image shows a recent solid model of the coudé laboratory. The beam comes to the lab from above M7 and is highlighted in yellow. M7 folds the beam at a 90-deg angle to be level with the lab floor. The entire laboratory is a rotating platform and is another degree of freedom for the optical system. Not all beams in all instruments are shown in the lower right hand solid model.

EST.[16,17] Figure 3 shows the optical beam on the lab floor, feeding all instruments. The optional CryoNIRSP feed is shown as a semitransparent line. All other instruments can be operated simultaneously with the adaptive optics.

In the optical modeling efforts, all three degrees of freedom (azimuth, elevation, coudé table angle) impact polarization calibration plans through the rotation of the projected image against the solar disk and subsequent rotation of polarization calibrations when tracking with images fixed to parallactic or solar coordinates. The azimuth and coudé table angles are redundant optically but do repoint the system celestially. We must consider the relative image rotation angle and time-dependent Mueller matrices when tracking the sun under a variety of use cases that either use or do not use the table angle.

When considering polarization performance of the optical system, the AOI variation as well as the variation across the FoV are both important considerations. As an example, the DKIST primary mirror converts a collimated beam from a single field angle to an $f/2$ converging beam. The effective fold angle for M1 is roughly 28.1 deg, but the bundle of rays exiting the optic sees fold angles between 14.3 deg and 41.1 deg across the beam footprint. The polarization properties vary strongly with AOI and this imparts polarization variation as a function of position in the beam leaving M1. Table 1 shows the variation in incidence angle for the on-axis (zero-field) beam in the design. The first column "optic name" lists the optic. The next four columns show the AOI for the chief ray of the beam, the marginal ray with maximum and minimum AOI, and the range of incidence angles. Subsequent columns of Table 1 show the effective $f/$number of the incoming and outgoing beams as well as the coating on the optic. The primary mirror is coated with bare aluminum, which quickly forms a thin oxide layer. All other mirrors M2 to the DM are coated with enhanced protected silver down to the coudé lab. These multilayer coatings tend to have stronger dependence on polarization properties with incidence angle and hence are important to model accurately across the full FoV. The wave front sensor beam splitter (WFS-BS1) has an uncoated front surface to feed the Fresnel reflection to the adaptive optics WFS. The coudé lab dichroic beam splitters CL *N* all have custom coatings to reflect some wavelengths while efficiently transmitting all other wavelengths. All beam splitters have an antireflection coating on the back surface optimized for their specific transmission wavelength region.

Whenever the pupil is demagnified, the field variation of incidence angles is increased accordingly. The incidence angle variation on the primary mirror is also the FoV angle.

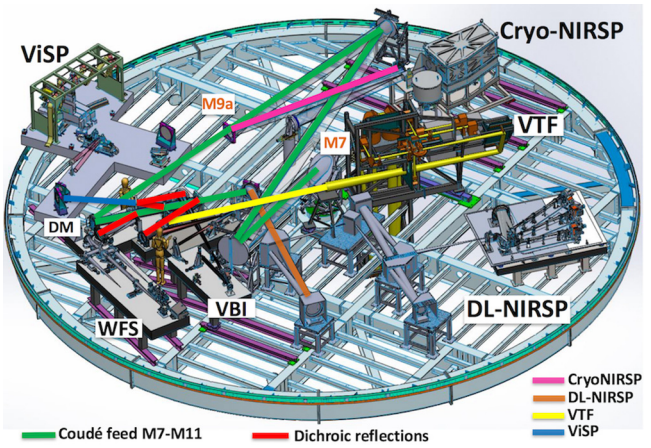

Fig. 3 The DKIST coudé laboratory and the various optical pathways feeding the instruments. The green line shows the coudé beam beginning from the reflection off the M7 flat. The M8 parabola collimates the beam and the beam is then folded by M9. There is a position labeled M9a where the optional CryoNIRSP pickoff flat can be inserted to feed all the light to CryoNIRSP following the magenta line. For all other instruments, the beam continues past the M9a station following the green line to the DM and is then AO corrected. There are several short red lines in a very confined space representing all the dichroic beam splitters. Ultimately these many reflections send different wavelengths to the polarimetric instruments (ViSP, VTF, and DL-NIRSP) along with the various camera and sensor systems (the adaptive optics WFS and the two high-resolution imaging cameras VBI-red, VBI-blue). The blue line shows the light path leaving the dichroic feeding ViSP. The rest of the ViSP beam is not shown on the ViSP optical bench. Yellow shows the light path leaving another dichroic feeding VTF. Orange shows a beam transmitting through the last dichroic and being reflected into DL-NIRSP.

Table 1 Optical properties of the DKIST on-axis beam with AOI.

Optic	AOI	AOI	AOI	AOI	$f/\#$	$f/\#$	Coating
Name	Chief	Max	Min	Range	In	Out	
M1	14.04	20.56	7.13	13.4	∞	2	Al – Al_2O_3
M2	11.84	17.27	6.03	11.3	2	13	Enh. Ag
M3	45	47.19	42.81	4.4	13	13	Enh. Ag
M4	1.76	2.57	0.93	1.6	13	53	Enh. Ag
M5	15	15.53	14.47	1.1	53	53	Enh. Ag
M6	30	30.53	29.47	1.1	53	53	Enh. Ag
M7	45	45.53	44.47	1.1	53	53	Enh. Ag
M8	5.33	5.60	5.06	0.5	53	∞	Enh. Ag
M9	10	10	10	0	∞	∞	Enh. Ag
DM	15	15	15	0	∞	∞	Enh. Ag
BS1	15	15	15	0	∞	∞	None
CL2	15	15	15	0	∞	∞	Dichroic
CL2a	15	15	15	0	∞	∞	Dichroic
CL3	15	15	15	0	∞	∞	Dichroic
CL3a	15	15	15	0	∞	∞	Dichroic
CL4	15	15	15	0	∞	∞	Dichroic

Note: The angle of incidence (AOI) for the on-axis (zero field) beam. The chief ray is traced through the system as well as the lowest and highest AOI for the marginal rays for the on-axis beam (zero FoV) on the optics. For instance, the primary mirror (M1) reflects the chief ray at 14.04 deg. Since M1 is a tilted off-axis parabola, the marginal rays are incident at angles between 7.13 deg and 20.56 deg representing a range of 13.4 deg AOI. The beam sees smaller AOI variation across the beam footprint in the $f/53$ portion of the relay. In the collimated beam after M8, there is no AOI variation across a footprint (zero field). The various dichroics combine in reflection and/or transmission to feed the beam to various instruments (see Figs. 2 and 3 as well as the text).

The optics demagnify the entrance pupil onto the DM, which is only 0.2 m across giving a 20× demagnification from the 4-m entrance aperture. We trace the incidence angle variation in Table 2 for the chief ray for every field point in the 2.8-arc min diameter field. As powered optics change the relationship between angles across the beam, we list the input and output variation for each powered optic where changes occur. The *Beam Loc* column in Table 2 shows the surface where AOI variation with FoV is computed. The next four columns show the field center incidence angle and the Min/Max incidence angles at the FoV edge. The FoV of the primary mirror is the nominal 2.8 arc min (0.05 deg). However, as the optics demagnify the beam, the incidence angles increase across the field. In the coudé lab, the pupil on the DM sees an incidence angle variation with FoV of 0.9 deg, roughly 20× the original 2.8-arc min FoV. It is apparent from Table 2 to see that the field variation is roughly one degree in all optics of the $f/53$ beam and in the collimated beam, which is the dominant source of field variation effects for polarization calibration.

2 Zemax Computations

Zemax traces individual rays in the Jones formalism through a geometric model. Zemax can propagate rays from any position in the entrance pupil at any field angle through the optical design. In Zemax, we have developed a script to trace polarized rays across the pupil and field while specifying a series of wavelengths, polarization states, and system optical configurations. We have adapted scripts initially developed by Harrington et al.[46]

The new scripts can change fold angles, rotation angles, wavelengths, etc., in order to provide the ability to simulate a wide range of optical system configurations. With this functionality, we can derive polarization properties of the system across the beam footprint for any desired setting on any desired surface in the system. We have recently applied this analysis to the 4-m AEOS telescope and compared the predictions to polarization calibrations derived from the daytime sky.[52]

Depending on the sensitivity and computational speed required, the pupil sampling, field sampling, wavelength coverage, and telescope pointing step size can be increased to sample the beam to a desired accuracy. Typically, sampling the footprint in a 20×20 grid of rays achieves <0.0001 level numerical precision, consistent with our simulation needs and is a good compromise between computation speed and numerical accuracy.

Table 2 Properties of the chief ray with FoV.

Beam	AOI	AOI	AOI	AOI	Beam
Loc.	(0,0)	Max	Min	w/FoV	$f/\#$
M1 in	14.00	14.02	13.98	0.05	∞
M2 in	11.84	11.93	11.76	0.17	2
M2 out	4.39	4.57	4.20	0.38	13
M3	45	45.19	44.81	0.38	13
M4 in	1.76	1.89	1.63	0.38	13
M4 out	3.52	3.98	3.07	0.90	53
M5	15	15.38	14.63	0.90	53
M6	30	30.38	29.63	0.90	53
M7	45	45.45	44.56	0.90	53
M8 out	10.66	11.11	10.22	0.90	∞
M9	10	10.45	9.54	0.90	∞
DM	15	15.45	14.55	0.90	∞
BS1	15	15.45	14.55	0.90	∞
CL2	15	15.45	14.55	0.90	∞

Note: The AOI variation with FoV. The table lists the incidence angle for the chief ray for every field point for the 2.8-arc min field propagating through the coudé lab and adaptive optics system. See text for details.

For other systems, more fine sampling may be desired when confronting more complex situations such as assessing vignetting at each field angle and, in general, the symmetries in the polarization properties of the final beam footprint when polarization analysis is performed.

The Zemax scripts output over 30 electric field vector components for every ray traced. The optical surface can also be specified to examine polarization properties on any optic in the design. To compute a Muller matrix from the Jones formalism, we independently trace a set of the six purely polarized inputs $\pm Q$, $\pm U$, and $\pm V$ through the system. For each of the six inputs, Zemax calculates the electric field properties in 3-D at the specified surface.

These electric field calculations are turned into Stokes vector formalism for each of the pure input states. The computed intensity is the square of the XY components of electric field amplitude $(ExEx + EyEy)$. Stokes Q is the X and Y amplitude difference: $(ExEx - EyEy)$. The term δ represents the phase difference and is one of the Zemax outputs but can also be computed directly as $\delta = \phi_x - \phi_y$. Stokes U is computed from X and Y electric field amplitudes accounting for coherent phase variations: $2ExEy\ \cos(\delta)$. Stokes V is similarly computed with both XY field amplitudes and phases: $2ExEy\ \sin(\delta)$.

We demonstrate Zemax polarization properties in this paper by computing the electric field distributions, Stokes vectors across various footprints and Mueller matrices for various optical systems. Figure 4 shows the articulation of the DKIST optical design from the primary mirror to the sixth mirror in the system (M6), which represents the optical configurations determining the azimuth–elevation pointing of the system as traced by our scripts. In the coming sections, we will show the Zemax computations for a simple flat fold mirror in a powered beam, and then a variety of surfaces within the DKIST design.

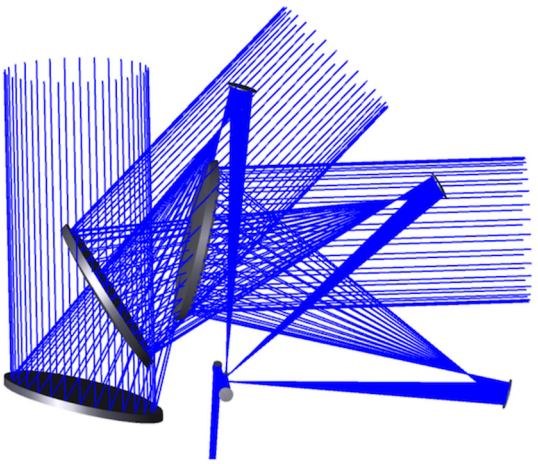

Fig. 4 The DKIST telescope design articulated in elevation. The off-axis $f/2$ primary mirror is seen in multiple locations as the telescope assembly pivots about the elevation axis.

3 Coating Formulations

The complex refractive index and thickness of each layer in a dielectric coating impact the polarization performance. For typical enhanced-protected metal coatings, there are one to several dielectric layers coated on top of the metal layer. Coatings are typically optimized for reflectivity over certain wavelength ranges but also be optimized for retardation and diattenuation.

Multilayer coatings can create two or more wavelengths where the retardation near the theoretical 180 deg for a perfect reflection. They can also introduce substantial retardation and diattenuation at other wavelengths, which depends strongly on incidence angles. The DKIST calibration plan presently groups the telescope feed optic Mueller matrices and reduces the number of variables required to predict the telescope Mueller matrix for all wavelengths, fields, and telescope pointings.[7,8,52] To create estimates of the likely DKIST Mueller matrix dependencies on field, telescope pointing, and wavelength, we need a model for the coating formula that captures the relevant dependencies on incidence angle and wavelength.

DKIST internal studies reported measurements of the retardation and reflectivity for witness samples across the 400- to 900-nm wavelength range. To estimate DKIST polarization performance, we needed our model coating formula to be representative of the expected retardance, diattenuation, and reflectivity.

Without access to a manufacturer-provided formula, we found a simple search of standard coating materials identified a reasonable formula for the coating that matched reflectivity, diattenuation, and retardance. For our polarization performance calculations, the retardance and diattenuation are important to match than the overall reflectivity. With an approximate coating formula, we can to estimate the amplitude of several polarization effects expected in DKIST. Having a formula allows us to estimate the expected dependence on incidence angle or FoV with

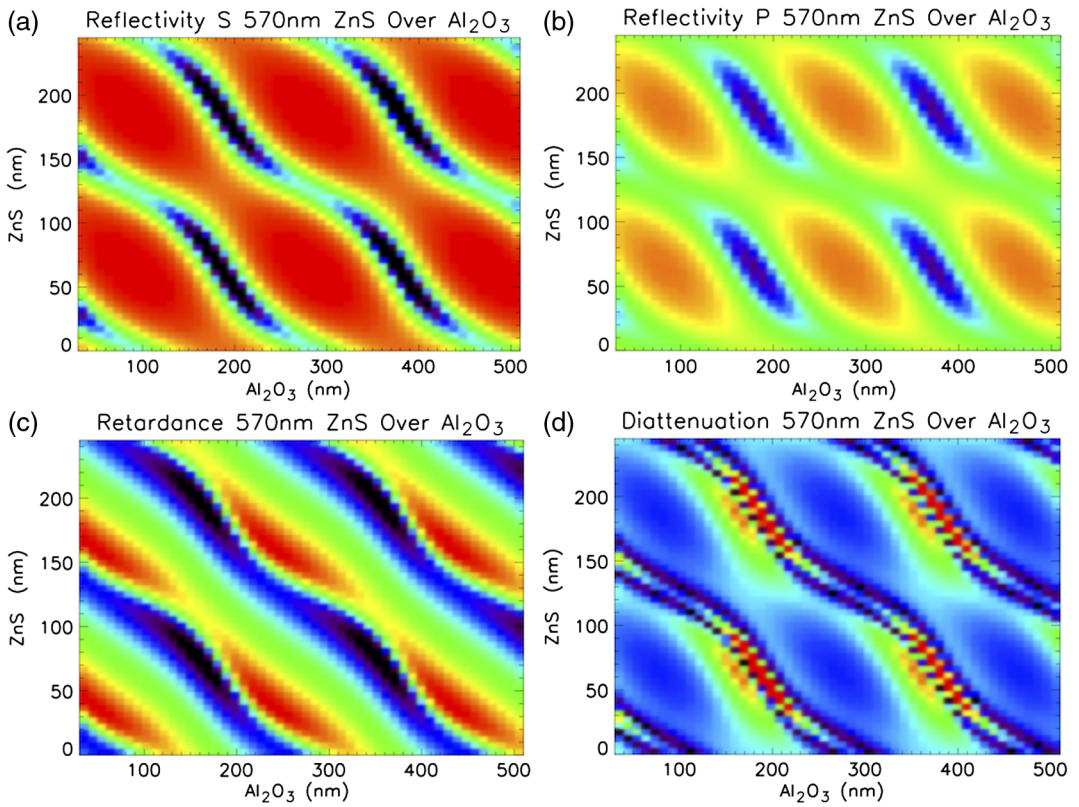

Fig. 5 The Zemax coating calculations as layer thickness are varied at 570-nm wavelength and 45-deg incidence angle. We ran a two-layer overcoating of zinc sulfide (ZnS)-coated over aluminum oxide (Al_2O_3) coated over the silver base coating. For each panel, we ran a grid of 50×50 thicknesses. The *x*-axis for every panel shows varying thickness of the aluminum oxide from 0 to 500 nm. The *y*-axis for each panel shows the thickness of ZnS from 0 to 250 nm. Note that for completeness, we ran models at half and double these scales (not shown here) to verify behavior of thicker and thinner layers. We also ran all combinations of ZnS, Al_2O_3, MgF_2, and SiO_2 (not shown here). (a) The reflectivity for the *S*-polarization state. The linear color scale runs from black at 85% reflectivity to red at 100% reflectivity. (b) The reflectivity for the P polarization state on the same color scale (85% to 100%). (c) The retardance. The linear color scale runs from black at 140 deg to red at 215 deg. (d) The diattenuation. The color scale goes from 0% for black to 3% for red. For all the plots, there are regions of high and low reflectivity, diattenuation, and retardance corresponding to the coherent effects of the coating layer thicknesses.

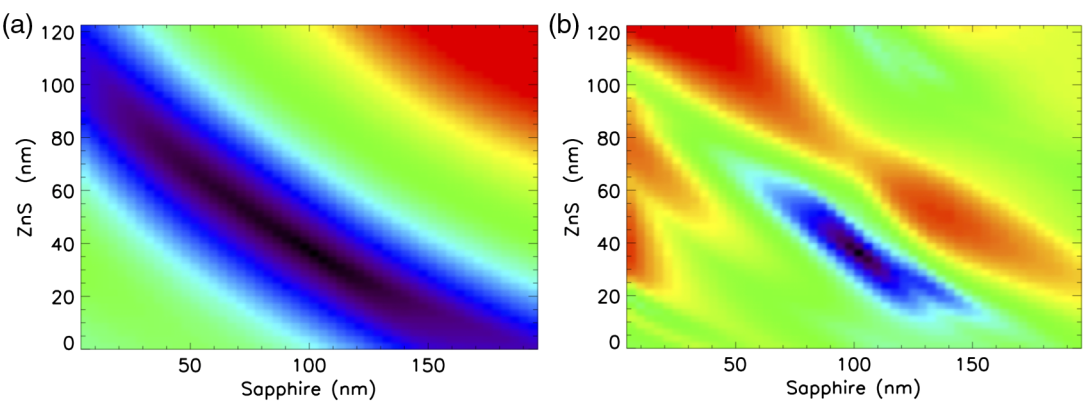

Fig. 6 The differences between a particular coating model and the various model coating formulas computed in Zemax for two example coating materials. The absolute value of the differences between retardances and diattenuations was summed over all wavelengths for every combination of material thicknesses. Low differences are color coded blue/black while large differences are red. (a) The difference between retardance values. (b) The difference between diattenuation values. Note that the behavior of diattenuation and retardance errors is quite different. We tested three common materials with one material coated over another for a total of six coating formulas.

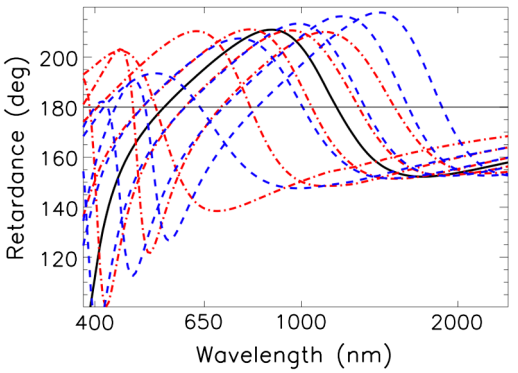

Fig. 7 The model retardance versus wavelength for selected coating layer thickness drawn from Figure 6. There are strong wavelength-dependent changes with even a few nanometer thickness variation. Black shows the nominal curve of 37.5-nm ZnS over 100 nm of Al_2O_3. The red curve shows variations in ZnS thickness over 100 nm of Al_2O_3. The blue curves show variations in Al_2O_3 with 37.5 nm of ZnS over coated.

reasonable amplitudes.[53] We wrote a Zemax script to output a coating polarization report for many combinations of material thicknesses allowing an efficient search of several possible coating formulas. For enhanced and/or protected silver formulas, fused silica (SiO_2), zinc sulfide (ZnS), magnesium flouride (MgF_2), and aluminum oxide (Al_2O_3) can be used as the protected layer. An example coating model run at 570-nm wavelength is shown in Fig. 5. Several additional coating formulas are shown in our recent publication.[52]

Often the harder materials (sapphire, fused silica) are used as the durable protective over-coating while other layers or materials are included to minimize retardance or maximize reflectivity at particular wavelengths with thickness tolerances of a few nanometer. All of the two-layer protective coating formulas shown by Harrington et al.[54] and the searches reported here do have two separate 180-deg retardance crossing wavelengths around 400 and 850 nm as was desired by the DKIST project.

We searched the common materials of ZnS, SiO_2, MgF_2, and Al_2O_3 in two-layer protective coatings over the metal layer. As an example of one of these searches, Fig. 6 shows a search of up to 200-nm aluminum oxide over a layer of up to 120 nm of zinc sulfide. Figure 7 shows variations in retardance for the reected beam with 5 nm changes in thickness of two dielectric layer thicknesses (ZnS and Al_2O_3). We identified a coating formula that has similar retardation, reflectivity, and diattenuation to our witness samples for the DKIST mirrors. This coating formula was not an exhaustive search of possible design space but simply a few iterations to achieve a reasonable match. For modeling efforts presented here, this coating formula will be useful to predict the system Mueller matrix for the CryoNIRSP instrument. We show the 1000- to 5000-nm wavelength range and select wavelengths for the ViSP instrument where the model coating formula matches the witness sample retardance.

Figure 8 shows the reflectivity, retardance, and diattenuation for this enhanced protected silver coating formula. For this coating design, there are two wavelengths where the 180-deg phase change from reflection is exactly met, but these points are functions of incidence angle. At lower incidence angles, the 180-deg retardance points shift to longer wavelengths. For the DKIST design, not all feed mirrors share the same incidence angle, so there will be no one wavelength where the telescope Mueller matrix is free of cross talk. There is a strong dependence on wavelength with 20-deg retardation amplitudes seen in the visible and near infrared at 45-deg incidence angles.

In addition, there are two wavelengths where the diattenuation is zero, but these two wavelengths are also functions of incidence angle. There will also not be any one wavelength where the telescope Mueller matrix is free of induced polarization. The actual coating formula from the various vendors providing the mirrors for all telescope and instrument optics are proprietary to the manufacturers. However, many enhanced dielectric protective coatings have at least 2 and in some cases many layers of material deposited on top of the metal. Additional adhesion layers also complicate the formula. We rely on these simple models to represent a close approximation to the polarization behavior as functions of the relevant variables.

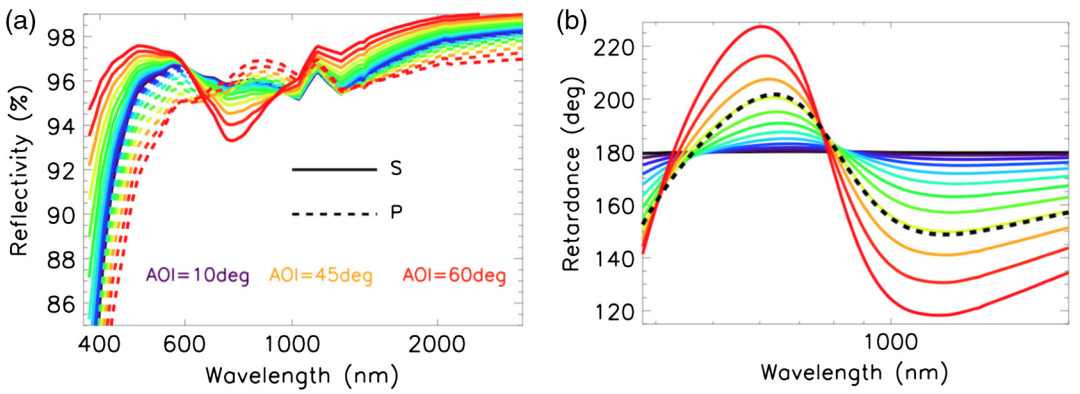

Fig. 8 The Zemax computed coating properties for the new enhanced protected silver coating formula as functions of incidence angle. Each color in each panel shows a different incidence angle from 0 deg to 60 deg in steps of 5 deg. Black is 0 deg, blue colors are 5 deg to 15 deg AOI and the red curve shows 60 deg AOI. (a) The *S* reflectivity as solid lines and the *R* reflectivity as dashed lines. The diattenuation is seen as the difference between the solid lines and dashed lines. Note how the diattenuation goes to zero at two separate wavelengths, and that those zero diattenuation wavelengths are functions of incidence angle. (b) The retardance as a function of wavelength for each incidence angle. The dashed black line shows 45-deg incidence. Retardance is a strong function of incidence angle. Also note how the retardance crosses 180 deg twice, but that the wavelengths of these zero points are a function of incidence angle.

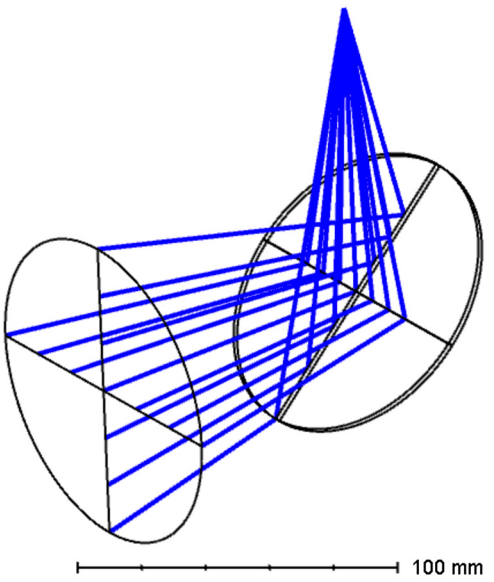

Fig. 9 The rays for the $f/2$ flat fold mirror at a 45-deg incidence angle.

4 Flat Mirrors

$$\mathbf{M}_{ij} = \begin{pmatrix} \frac{1}{2}\left(1+\frac{R_p}{R_s}\right) & \frac{1}{2}\left(1-\frac{R_p}{R_s}\right) & 0 & 0 \\ \frac{1}{2}\left(1-\frac{R_p}{R_s}\right) & \frac{1}{2}\left(1+\frac{R_p}{R_s}\right) & 0 & 0 \\ 0 & 0 & \sqrt{\frac{R_p}{R_s}}C_\delta & \sqrt{\frac{R_p}{R_s}}S_\delta \\ 0 & 0 & -\sqrt{\frac{R_p}{R_s}}S_\delta & \sqrt{\frac{R_p}{R_s}}C_\delta \end{pmatrix}. \tag{1}$$

We present in this section some simple Zemax computations with flat mirrors. These calculations are readily comparable with theory and various lab tests. Most optical ray tracing programs, including Zemax, will output reflectivity, diattenuation, and retardance for a single-coated surface. The theoretical calculation involves three parameters. R_s is the reflectivity in the S-plane (German: senkrecht, meaning perpendicular). R_p is the reflectivity in the P-plane (German: parallele meaning parallel).

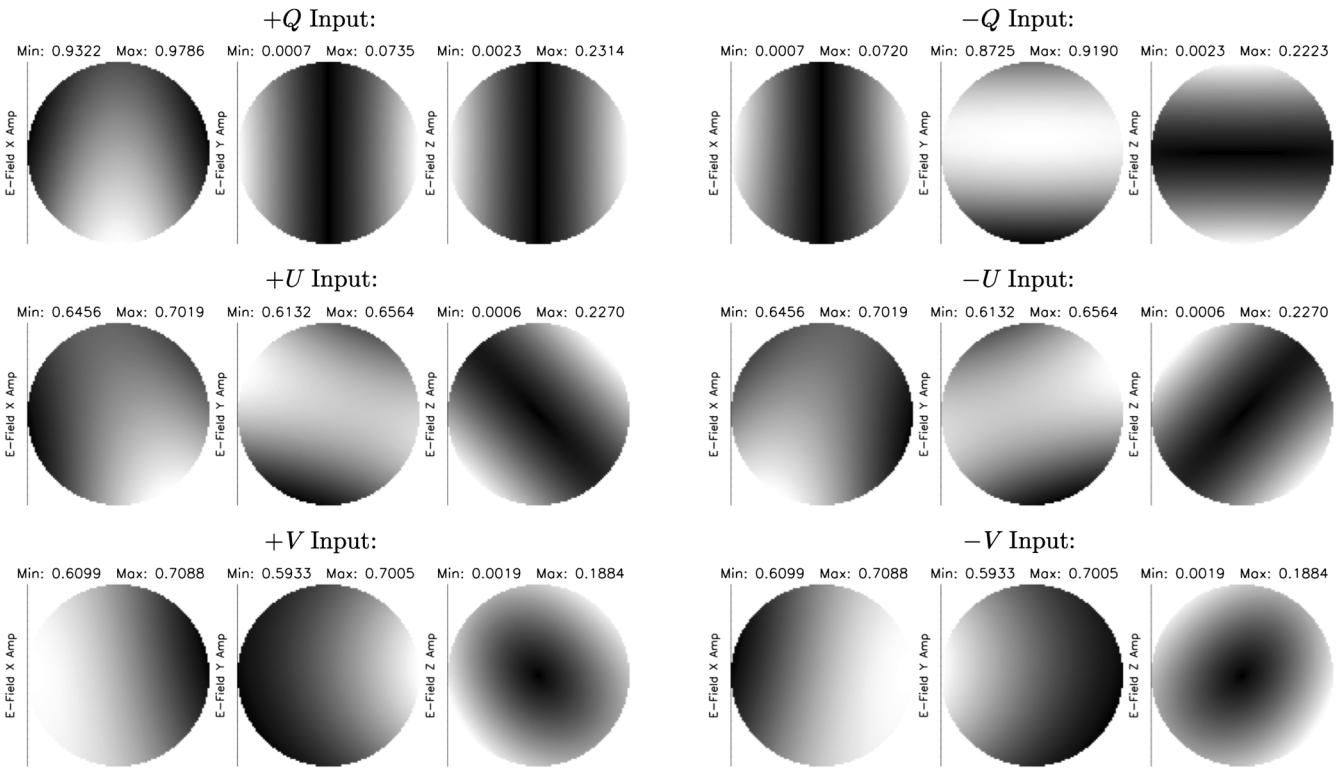

Fig. 10 Electric field component amplitudes calculated across the beam footprint for a flat fold mirror in an $f/2$ beam set at 45 deg AOI on the chief ray of the system shown in Fig. 9. The Jones matrix corresponding to the fully polarized pure Stokes inputs were specified and traced using our scripts to the focal plane of this $f/2$ beam. Each panel shows a linear gray scale of the XYZ electric field amplitude from the minimum to maximum listed above each panel. As an example, the top left corner shows the amplitude of the X component of the electric field when a pure $+$Q input state is traced through the system linearly scaled from $+0.9322$ to $+0.9786$. This mirror has a reflectivity of 0.9342 for the S- state at a 45-deg incidence angle but in the $f/2$ beam, the incidence angles vary from 30.96 deg to 59.04 deg. The Y field amplitude is below 0.074. The Z-field component is below 0.23. The top right three panels show the $-Q$ input state. This represents the $-P$ beam with a reflectivity of 84.33% at an AOI of 45 deg. Variation is seen in the Y field amplitude from 0.87 to 0.92. The Z-field component has changed orientation but has the same amplitude as the $+Q$ input. The X amplitude for $-Q$ input looks like the Y amplitude for the $+Q$ input. Similar changes in orientation and sign are seen for the $\pm U$ and $\pm V$ input states. A clear pattern is that the XY field amplitudes are much higher for the $\pm Q$ input states, whereas the U and V inputs show a mix between field amplitudes. The UV and VU Mueller matrix elements are $\sim$0.33.

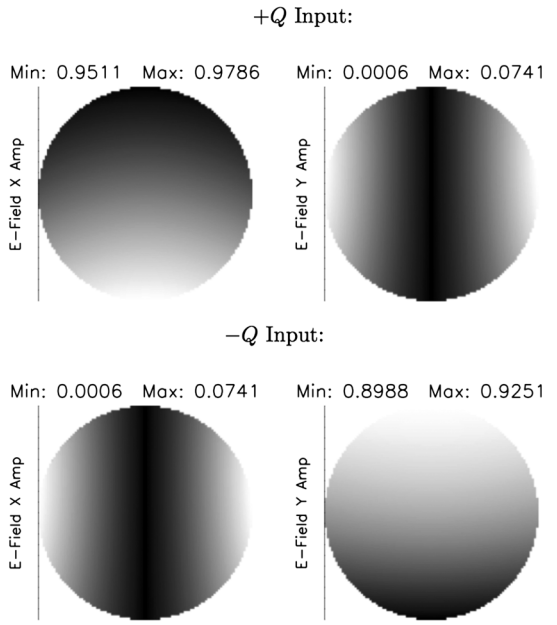

Fig. 11 The electric field components calculated across the beam footprint similar to Fig. 10 but after a paraxial collimating lens was placed near focus. With the collimated beam, the Z component of the electric field is zero. We only show $\pm Q$ input states here for comparison with Fig. 10. The $+Q$ input state electric field component for X ranges from 0.951 to 0.979 here, whereas it was from 0.932 to 0.979 in the $f/2$ system of Fig. 10.

The retardance is denoted as δ. With the notation of C_δ and S_δ denoting cosine and sine, respectively, a simple Mueller matrix for a single-flat fold mirror in a collimated beam is computed via Eq. (1).

DKIST staff and others in the literature have used simple Mueller matrix formulas based on a single ray at a single-fold angle to estimate Mueller matrix properties.[55] In Zemax, a flat mirror in a collimated beam represents that approximation and should reproduce the simple Mueller matrix dependencies found with simple theory.

4.1 *Converting Electric Fields to Mueller Matrices in Converging Beams*

A flat fold mirror model was created in Zemax. A paraxial 200-mm focal length lens was inserted at the 100-mm diameter system stop. This 100-mm diameter beam comes to focus after 200 mm of propagation and is an $f/2$ system. As the entire system is paraxial, the rms spot size at the focal plane is zero within numerical accuracy. There are no geometrical aberrations in the system. The fold mirror was set to an incidence angle of 45 deg corresponding to a 90-deg fold. The mirror was placed half way between the stop and focal plane, corresponding to 100 mm of propagation between the stop and the focus. Figure 9 shows the system layout. For an $f/2$ fold, the incidence angles vary from 30.96 deg to 59.04 deg.

We demonstrate the conversion between electric field vectors and Mueller matrices by using a converging $f/2$ beam reflecting of a flat fold mirror at 45-deg incidence angle.

We computed Mueller matrices for this fold mirror with one of our enhanced protected silver formulas. The II and QQ elements of the Mueller matrix were 0.9513. When the Mueller matrix was normalized such that $II = 1$, the IQ and QI terms were 0.0513, the UV and VU terms had an amplitude of 0.3238 with the UU and VV terms at 0.9447. The coating analysis in Zemax agreed with these electric field calculations. A fold at 45-deg incidence angle with this coating gave a retardance of 161.1 deg, a diattenuation of 0.0513 and R_s was 93.42%, whereas R_p was 84.33%.

Following the formula in Fig. 1 and using the computed reflectivities from the Zemax coating file, we recover the same Mueller matrix computed from the electric fields. This shows consistency between the mathematics used in the Zemax coating computations and our electric field calculations. Note that with incidence angles varying from 30.96 deg to 59.04 deg across the footprint, there will be strong variation in the derived Mueller matrices.

The scripts produce the electric field real and imaginary components from which we compute the XYZ components of the electric field across the footprint. In our case for this $f/2$ converging beam, the rays all converge to the focal plane and as such are spatially overlapping. Figure 10 shows the XYZ electric field amplitudes when all pure Jones vectors are input (representing the six fully polarized pure Stokes inputs).

Zemax propagates rays in the Jones formalism by a specified optical path length along a computed propagation direction. When the electric field distribution is computed, the xyz coordinates represent that of the global xyz coordinates computed for the system at that location in space. In Fig. 10, there are substantial Z components to the electric field for all nonchief rays.

In any real polarimeter, the performance of the analyzing polarizer, beam splitter transmission functions, reflection coefficients, etc., will all be substantially different than if one simply simulates the behavior of the chief ray. As a simple computational aide, we collimate the incoming $f/2$ beam with a paraxial lens. When collimated, the Z component of the electric field went to zero. The electric field computation we outlined above, the Mueller matrix is derived from the Stokes parameters considering only the XY components of the electric field. In most situations, the Z component of the field is small as the $f/$number of the beam in the polarimeter is typically greater than 10. A more detailed computation with the full 3-D electric field distribution is possible and will be explored in future works.

The properties of the Mueller matrix change substantially with the $f/$number of the beam. When considering the normalized Mueller matrix with only the fold at 45 deg, the IQ and QI terms were 0.0513, the UV and VU terms had an amplitude of 0.3238 with the UU and VV terms at 0.9447. When summing over the footprint in the $f/2$ beam, we see a mild increase in the IQ and QI terms to 0.0517. The UV and VU terms change by about 5% to 0.3065 amplitude. The UU and VV terms also change to 0.9492.

In addition, the QQ term is no longer identical with the II term. In the normalized Mueller matrix, all terms are divided by II but the QQ term is 0.9968 after normalization, showing some depolarization. The diattenuation, depolarization, and retardance of the system can become much more complex than the formula for a simple single fold mirror.

We should note that the variation in electric field properties seen in Fig. 10 is dominated by AOI variation across the mirror. We have run calculations where we use a second paraxial lens near the focal plane to collimate the system. As expected, the Z component of the electric field goes to zero. Figure 11 shows the amplitude of the X and Y electric field components when the

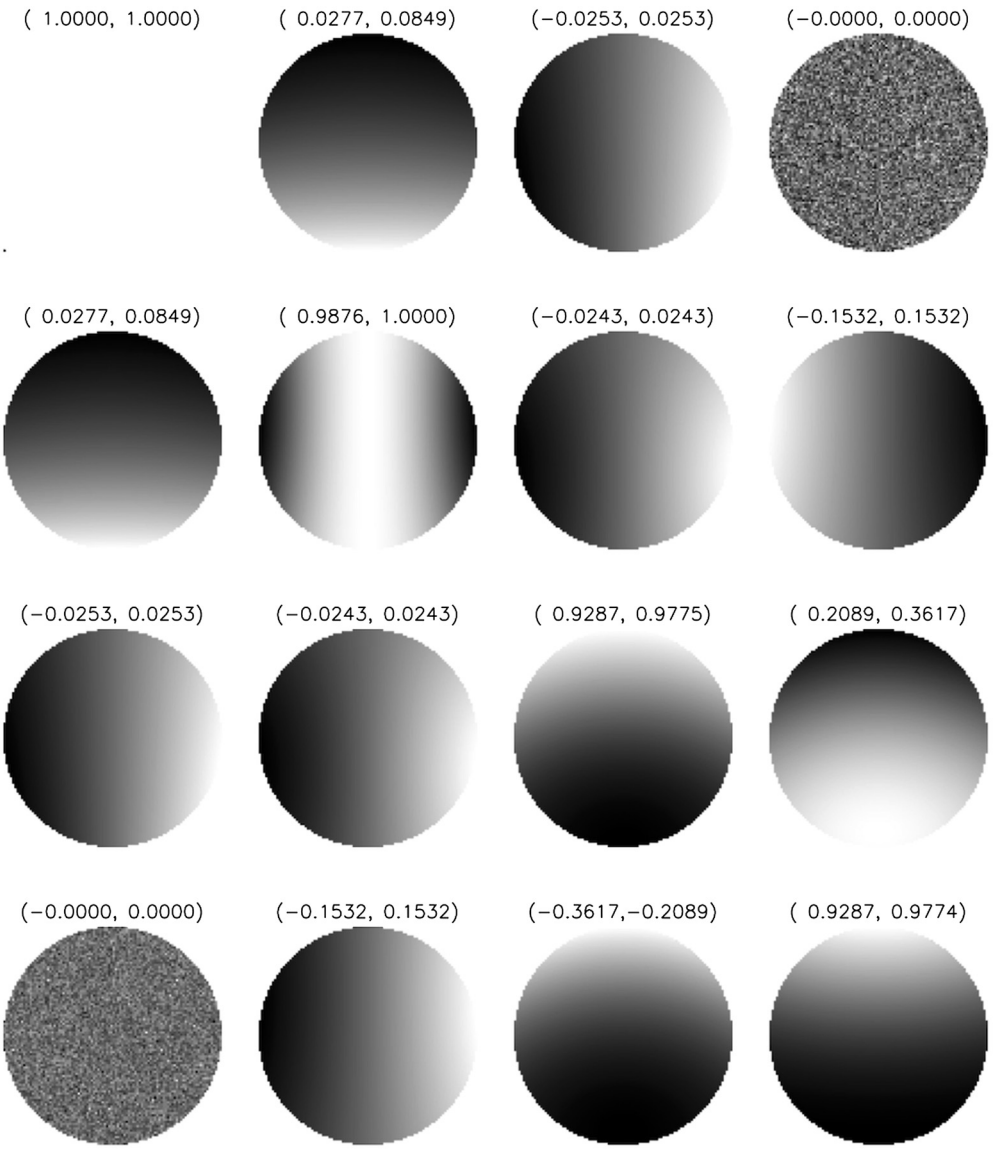

Fig. 12 The Mueller matrix across the beam footprint for the $f/2$ fold normalized by the intensity. The Stokes vectors were computed after paraxial collimation near the focal plane to set the Z component of the electric field to zero. The incidence angles vary from 30.96 deg to 59.04 deg along the extreme marginal rays reflecting off the fold mirror but the incidence angles are set to zero across the footprint on the focal plane by the collimating paraxial lens. The intensity normalization is done for each ray independently and the II elements ran from 0.855 to 0.888. Each panel shows the Mueller matrix element with the linear gray scale limits from min to max. The QQ term is always above 0.9876. The UV term has amplitudes ranging from 0.21 to 0.36.

converging beam is collimated near focus. The Z component of the electric field is zero. With the symmetries of the Z field component and the use of both the $+$ and $-$ Stokes inputs to derive the system Mueller matrix, the numerical values of the Mueller matrix are the same whether the system is collimated or converging $f/2$.

Figure 12 shows the derived Mueller matrix from the $f/2$ fold computed after a collimating paraxial lens, which sets the Z component of the electric field to zero for all rays. Note when the system is not collimated on the optical surface evaluated, there is an asymmetry between the top row of I to QUV terms and the first column of QUV to I terms in the derived Mueller matrix. As an example, this $f/2$ fold gives the Mueller matrix in Fig. 12 when collimated but when at $f/2$, the VI term ranges about $\pm 1\%$ while the IV term is unchanged and is zero with numerical precision limits.

As we use only the XY components of the electric field to compute the Stokes vectors from the Jones formalism, we make an error in steeply converging beams. A real polarimeter uses an optic to analyze the beam, propagating some components of the electric field vector that also vary strongly with incidence angle and the type of optic used. An open question to be investigated in future work is what the limits are as a function of $f/$number on a real analyzer. For the time being, we will only convert from Jones to Stokes in slow systems such as $f/200$ for AEOS, $f/40$ for HiVIS, $f/26$ for ViSP presented below.

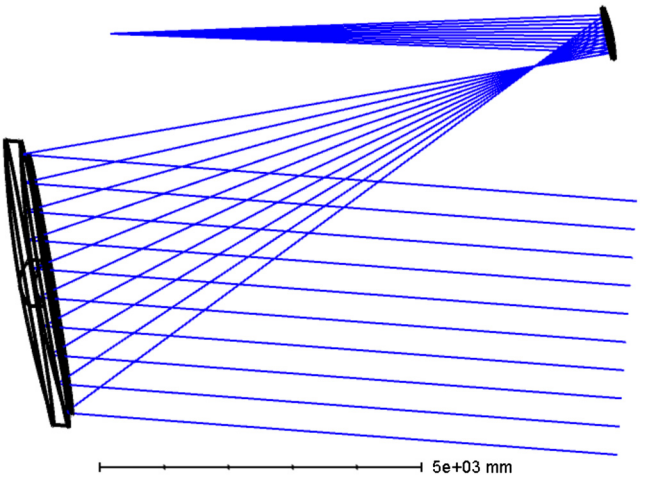

Fig. 13 The on-axis rays for the beam entering the telescope and propagating to Gregorian focus. The 4.24-m primary mirror with the 4.0-m entrance aperture is seen creating the $f/2$ prime focus. Incidence angles on M1 range between 7.13 deg and 20.56 deg. The incidence angles range by ± 2.2 deg across the $f/13$ beam at Gregorian focus.

4.2 *Aluminum Oxide Coatings and Comparisons with Flat Mirrors Reflections in the DST*

The Zemax model predictions change drastically in response to changing coating formulas. Small changes in the refractive index, absorption coefficients, or thicknesses of protective layers can change the diattuenation by >1% and retardance by many degrees. If the retardation and reflectivity of the coating formula for the DKIST mirrors are not matched in detail, the system performance predictions will be inaccurate. For off-axis, high AOI systems like DKIST, the coating performance must be accurately measured with the incidence angle to be modeled correctly as a formula.

Modeling of aluminum metal coating and the aluminum oxide layer that forms over top is important for computing system reflectivity and polarization performance. Aluminum oxide has the same chemical formula as sapphire (Al_2O_3) but with an amorphous (noncrystalline) structure and different birefringence properties. Various studies have been done on the polarization and reflective properties of aluminum and aluminum oxide compared to standard optical constants handbooks.[34,46,47,55,56]

From the Dunn Solar Telescope (DST) staff, a formula was derived as 872 nm of aluminum over 40 nm of aluminum oxide by fitting the telescope polarization model (courtesy of David Elmore, private communication). Models from Socas-Navarro et al.[34] derive the mirror optical constants along with other properties from fits to the telescope Mueller matrix.

In this DST coating formula, the aluminum has a complex refractive index specified at many wavelengths. Certainly many other formulas are easily considered in response to other studies and with our own ellipsometer.[55] An early DKIST study we performed also used (0.667, −5.57) and (0.7 −7.0) for the aluminum refractive index. Note that in studies by Harrington on the AEOS telescope,[46,47] the aluminum index of refraction was shown to have strong polarimetric impact. For DKIST as shown later, the aluminum oxide is only on M1, whereas the enhanced protected silver coatings dominate the system polarization behavior.

Van Harten et al.[55] found thickness of 0.5 to 4 nm of oxide. This is in contrast to the 40 to 50 nm used in studies at the Dunn Solar Telescope.[34] We note that the wire grid polarizers we use have a wire thickness of <40 nm and a pitch of 80 nm such that the entire wire would oxidize and cease to function if values like 40 nm were realistic.

For this study, we are simply demonstrating the impact of coatings on polarization performance predictions. The predicted aluminum reflectivity versus wavelength is roughly similar to other models when using the refractive indices and coating layer thicknesses reported here. The interpolation between wavelengths in this DKIST coating file is also apparent due to the coarse wavelength sampling, but the overall behavior shows the expected reflectivity of 82% to 87% in the 380- to 900-nm wavelength range.

To test this work against earlier DKIST performance predictions, we use 500-nm wavelength, 45-deg AOI (a 90-deg fold angle), 1.625 real index for the oxide, and (0.6667, −5.5726) refractive index for the aluminum following internal DKIST reports. The resulting transmission is an exact match at 87.22%. The reflectance for R_s is 88.90% and R_p is 85.53% with the phase (δ) of 2.53 deg, which also exactly matches Eq. (1). The derived Mueller matrices follow Eq. (1) to many decimal places showing that we do reproduce the theoretical equation within good limits. For an 80-deg fold at a wavelength of 500 nm, the oxidized aluminum gives 86.85% transmission, IQ and QI terms of 1.54%, UU and VV terms of 0.8918 amplitude, UV and VU terms of 0.4522 amplitude and follows the theoretical equation. The intensity to linear polarization and linear polarization to intensity terms are a few percent. Properties of aluminum-coated fold mirror pairs can be compared with the common *turret* style solar telescopes of the DST, the German Vacuum Tower Telescope[29,41,42] and are common in designs of other solar telescope optical relays.[16,36,57]

5 DKIST Gregorian Focus

Zemax calculations were performed to compare the baseline DKIST coating files against early reports and predictions for the Gregorian focus Mueller matrix. The oxidized aluminum formula is coated on M1, whereas an enhanced protected silver formula is coated on M2. The total intensity is around 0.87- at 500-nm wavelength, which includes reflection losses by coatings (mostly from aluminum at that wavelength). Figure 13 shows the layout of the first two DKIST mirrors and the beam to Gregorian focus.

An internal 2002 DKIST report showed calculations and trade-offs for the polarization of prime and Gregorian focus concluding that the field dependence was well below calibration limits and was thus negligible. This working assumption was carried forward in all DKIST documentation and is also supported here. The 2002 report was based on an $f/30$ Gregorian focus design, though the present DKIST design is now at $f/13$. However, the report concluded that variation across the Gregorian FoV was negligible. "The off-axis elements are all well below 10^{-5}, and therefore, no calibration would be needed even at 2.5 arc min away from the center of the field-of-view."

The properties of the current $f/13$ Gregorian focus are investigated below. Table 3 shows the Mueller matrix computed by the scripts for an $f/13$ beam and a slow beam (effective $f/30$) at 400-nm wavelength. The total transmission ranges from 72.05% to 72.76% across the footprint. The Mueller matrix elements in the $f/13$ beam have some small amplitude elements (UI, IU,

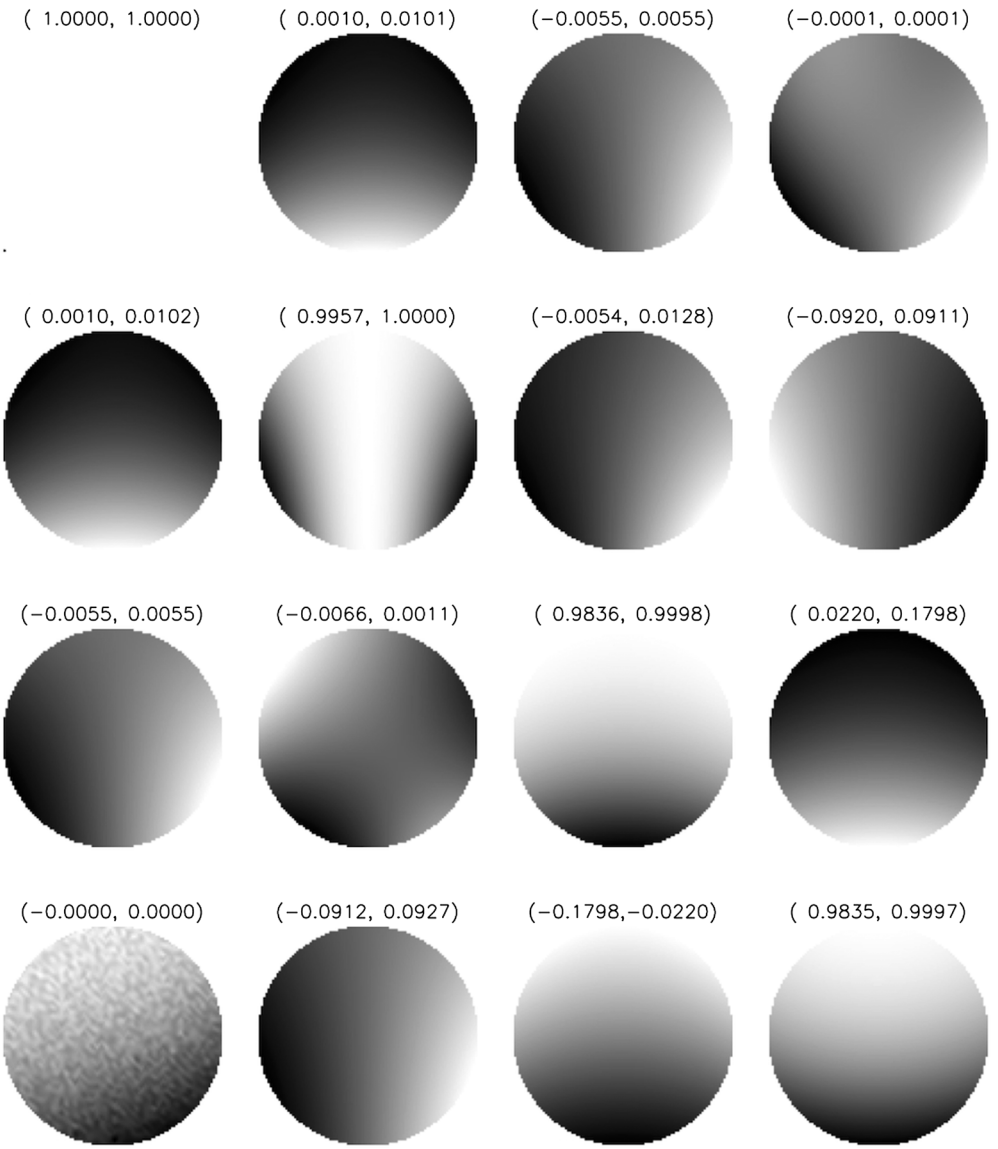

Fig. 14 The Mueller matrix at 400-nm wavelength across the beam footprint for the $f/13$ Gregorian focus of DKIST for the on-axis (zero field) beam. M1 was coated with the DST aluminum oxide formula. M2 was coated with our enhanced protected silver formula. The Stokes vectors were computed in the $f/13$ beam ignoring the Z component of the electric field vector. The incidence angles vary by ± 2.2 deg along the extreme marginal rays of the $f/13$ beam. In addition, the beam at a radius of 2.5-arc min is incident at a 0.33-deg angle on the field edges. Marginal rays will thus see an asymmetry going from ± 1.8 deg to ∓ 2.5 deg. The intensity normalization is done for each ray independently and the II elements ran from 0.720 to 0.727 accounting for the reflectivity of the oxidized aluminum and enhanced protected silver. Each panel shows the Mueller matrix element with the linear gray scale limits from min to max. The QQ term is always above 0.9957. The UV term has amplitudes ranging from 0.022 to 0.180. As the Z component of the electric field was ignored, there is some residual VI term error of 0.0001 caused by this assumption in an $f/13$ beam. A separate computation with a collimating paraxial lens near Gregorian focus working $f/36$, paraxial $f/74$ reduced this to 10^{-5}.

QV, VQ, QU, UQ) that are not present in the theoretical formula for a reflected Mueller matrix. However, neglecting the Z electric field component influences some components of the Mueller matrix at $f/13$. For the $f/30$ beam calculation in the lower half of Table 3, these elements go to zero. There are still some depolarization terms even when the calculations are done in a paraxially collimated system. The IQ and QI terms are 0.45%, the QQ term is not 1, and the UV, VU terms have 0.0847 amplitude. This depolarization originates in the averaging over the aperture.[49,58–62] Figure 14 shows the Mueller matrices varying across the footprint of the Gregorian focus beam. Substantial variation is seen along with some asymmetries.

The Mueller matrix computed for Gregorian focus at 400-nm wavelength, $f/13$ above, $f/30$, and collimated below. Depolarization is seen $\sim 0.1\%$ in the diagonal as $QQ \neq 1$ and $UU \neq VV < 0.9964$ as $\cos[\sin^{-1}(0.0847)]$.

We compute Mueller matrix variation for both the on-axis footprint and the 5-arc min field. As expected for an $f/2$ off-axis system, there are substantial asymmetries in the

Table 3 Gregorian focus Mueller matrix.

1.0000	0.0044	0.0001	0.0000
0.0044	0.9991	−0.0028	0.0007
0.0001	0.0028	0.9956	−0.0841
0.0000	−0.0004	0.0842	0.9946
1.0000	0.0045	0.0000	0.0000
0.0045	0.9991	0.0000	0.0000
0.0000	0.0000	0.9955	−0.0847
0.0000	0.0000	0.0848	0.9946

footprints for all field angles. However, most of the Mueller matrix terms are symmetric and largely average to zero after reflecting off the M1–M2 mirror pair. As concluded in a 2002 DKIST report, the Mueller matrix variation across the 5-arc min FoV is at the 10^{-5} amplitude level and is well below other DKIST calibration issues.

We show the expected amplitude of some Mueller matrix elements in Fig. 15. The IQ and QI terms show a higher amplitude at short wavelengths, caused by the silver, and a peak at 800 nm of about 0.5%, caused by the aluminum. Similar effects are seen in the amplitude of the UV and VU elements on the right side of Fig. 15. The matrix element is above 0.08 at short wavelengths and falls toward the visible band but again rises in the NIR, mostly caused by the silver coating.

6 CryoNIRSP Predictions with Pointing, Wavelength, and Field

We created polarization models for all optics feeding the CryoNIRSP instrument as functions of wavelength, telescope pointing, and FoV. Figure 16 shows top and side views of the coudé lab solid model and the optical design for the coudé lab optics between the seventh mirror (M7) and the CryoNIRSP modulator. We used the enhanced protected silver coating on all the DKIST optics from M2 to the CryoNIRSP modulator. As the CryoNIRSP instrument requires inserting a fold mirror, the beam path to CryoNIRSP is all-reflective. Though the coatings for CryoNIRSP optics are not yet completed, we anticipate that the coating formulas presented here will be used on all relevant CryoNIRSP optics. The telescope azimuth, elevation, and wavelength were varied in the scripts to articulate the system as in Fig. 4.

The Zemax models were computed at wavelengths of 500 to 5000 nm in steps of 500 nm. The telescope azimuth and elevation were computed over the full hemisphere in steps of 2 deg to capture the complete (Az, El) behavior of the system Mueller matrix.

The computation was done in a coordinate reference system that is tied to the entrance pupil of the optical train. This causes the definition of the QU coordinate grid to rotate as seen from the perspective of a fixed XYZ frame where the Mueller matrix is computed. This means that, in addition to any circular retardance in the system, there is a purely geometrical rotation from a QU reference frame at a downstream optic to a QU input frame in the entrance aperture of the Zemax optical design.

Figure 17 shows the system Mueller matrices as functions of azimuth and elevation at the CryoNIRSP modulator for wavelength of 2500 nm for the on-axis beam. All 16 elements of the Mueller matrix are shown with azimuth on the X-axis and elevation on the Y-axis in their own box. Each box is linearly scaled to highlight the azimuth–elevation dependence of the individual Mueller matrix elements. Each Mueller matrix has been normalized by the transmission at each individual telescope pointing so the (0,0) element is always 1.

As the DKIST relay is a series of fold mirrors articulated in azimuth and elevation, there is a simple functional form of the Mueller matrix. Each Mueller matrix element can be represented as sin and cos functions of azimuth, 2 ∗ azimuth, elevation, and 2 ∗ elevation. This is caused by the crossing and uncrossing of the incidence planes of the various fold mirrors between the azimuth and elevation rotation axes. This is also the same behavior as shown for the AEOS telescope.[52] In that paper, on-sky calibrations were used to derive the system Mueller matrix, and the functional dependence was easily fit with simple trigonometric functions.

In Fig. 17, the QUV to QUV terms are linearly scaled to amplitudes of ±1. The QU to QU terms contain both the

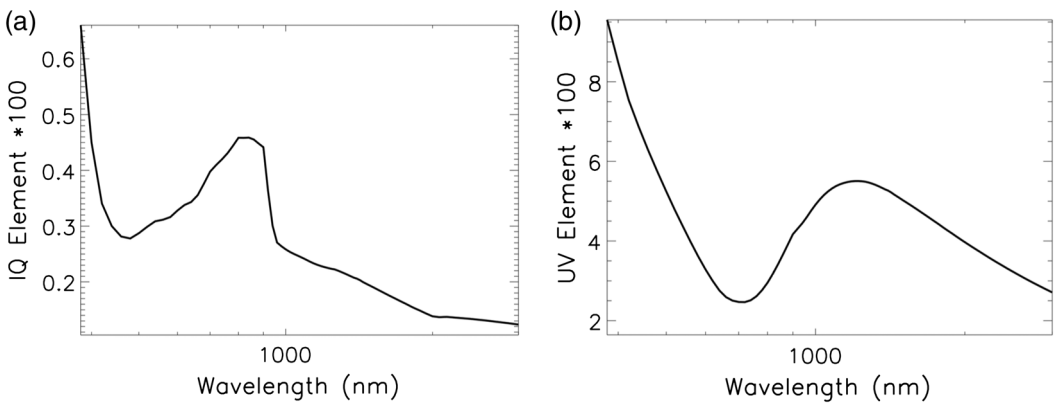

Fig. 15 The Zemax computed (a) IQ and (b) UV Mueller matrix elements for the on-axis beam at Gregorian focus. The oxidized aluminum coating was used on M1 and the enhanced protected silver formula was used on M2. Aluminum is less reflective around 800-nm wavelength and this creates an increase in diattenuation. Both coatings have wavelength-dependent retardance, which creates similarly complex behavior with wavelength in the UV element of the Mueller matrix.

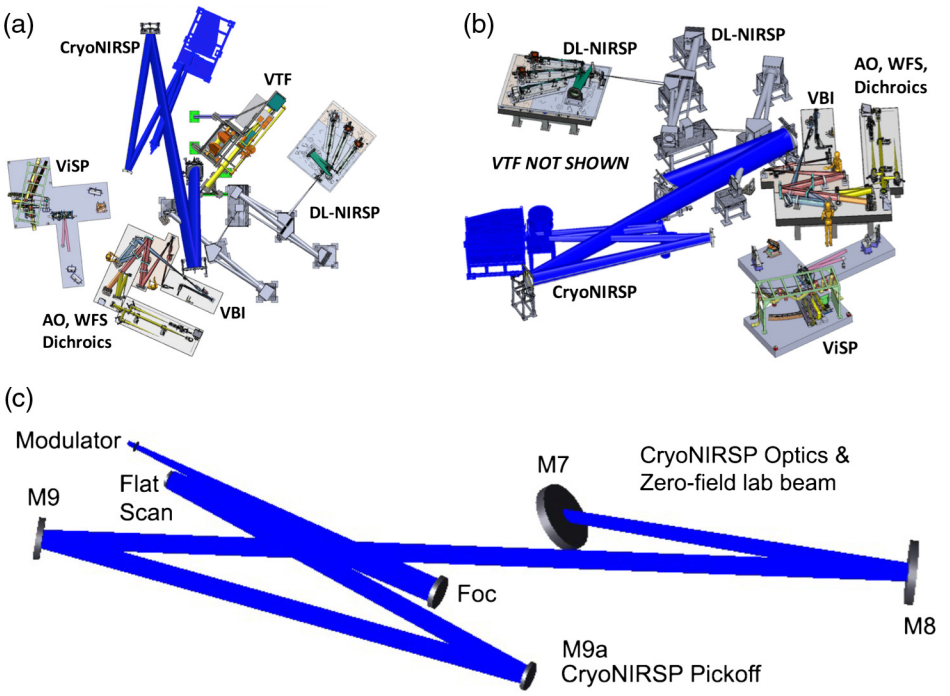

Fig. 16 The CryoNIRSP feed optics on the coudé floor from M7 through the modulator. (a) A solid model of the coudé lab instruments with the beam and CryoNIRSP highlighted in blue. (b) The solid model from a side view again with CryoNIRSP and the beam highlighted in blue with the VTF instrument removed for clarity. The solid models have the ViSP beam removed for clarity. (c) The optical model with zero FoV. M7 folds the incoming $f/53$ coudé beam parallel to the lab floor. M8 is an off-axis parabola that collimates the beam, which is then folded by M9. The M9a pickoff flat mirror is an enhanced protected silver fold that is inserted to feed all light to CryoNIRSP. The CryoNIRSP instrument optics include a beam splitter at 9-deg incidence angle, a scanning mirror at 4-deg incidence angle and another off-axis parabola at very small angle to accomplish focusing on to the slit through the modulator. The scanning mirror can repoint the instrument against the incoming beam, effectively decentering the beam of this slit instrument to off-axis footprints on upstream optics.

geometric rotation from the coordinate system and also any possible circular retardance. The intensity to QU terms and the QU to intensity terms (IQ, QI, IU, UI) are scaled to $\pm 1\%$ and show strong cos $(2 * \mathrm{Az})$ dependence along with elevation variation. The IV and VI terms are scaled to $\pm 0.2\%$ and show similar functional dependence. These terms reach their maximum amplitudes at some (azimuth, elevation) combinations with zero amplitude seen in specific elements only at specific telescope pointings.

Given the slowly varying retardation and diattenuation of the coating formula in the 1500- to 5000-nm wavelength range from Fig. 8, the differences between wavelengths are mostly seen as an amplitude change of the induced polarization terms. Figure 17 shows representative of the azimuth–elevation behavior for the Mueller matrix at all near-infrared wavelengths coming into the CryoNIRSP modulator.

6.1 *Field and Wavelength Variation*

Select Cryo-NIRSP Mueller matrix elements at a telescope azimuth, elevation combinations of 0 deg and 45 deg are shown in Fig. 18. The wavelength dependence is dominated by the model coating formula and the relative geometry between the groups of mirrors in the DKIST design.

The predictions are generally limited by the wavelength sampling of the vendor-supplied coating data. The coating files specified have coarse sampling in the near-infrared spectral region, leading to some linear behavior with wavelength in Fig. 18. Since mirror pairs can rotate an incoming Q signal into the UV cross-talk term of a subsequent mirror, Fig. 18 shows that some azimuth, elevation combinations have minimal UV dependence regardless of the coating retardation.

If the FoV dependence is above calibration requirement amplitudes, we have to add additional variables to the calibration plans. Figure 19 shows the variation from field edge to field center of the QUV to QUV Mueller matrix elements for a full 5-arc min FoV. Azimuth, elevation combinations of (0 deg, 45 deg) are used at left and (45 deg, 0 deg) are used on the right. The variation reaches amplitudes of up to 0.02 with a strong dependence on telescope pointing. The wavelength dependence generally follows the retardance formula for the coating combined with the geometric effects of one mirror rotating a linear polarization signal into the UV cross-talk axis of another mirror. In general, this causes strong QUV to QUV rotations.

7 Visible Spectro-Polarimeter

The ViSP uses several reflections and transmissions through a train of beam splitters. The beam splitters can be antireflection coated windows, mirrors, and/or dichroic beam splitters. We chose here to show the Mueller matrix of the beam delivered to the modulator inside this instrument. The beam path on the coudé lab floor is shown for ViSP in Fig. 20. We use the DKIST feed optics with an all-mirror feed to ViSP with azimuth

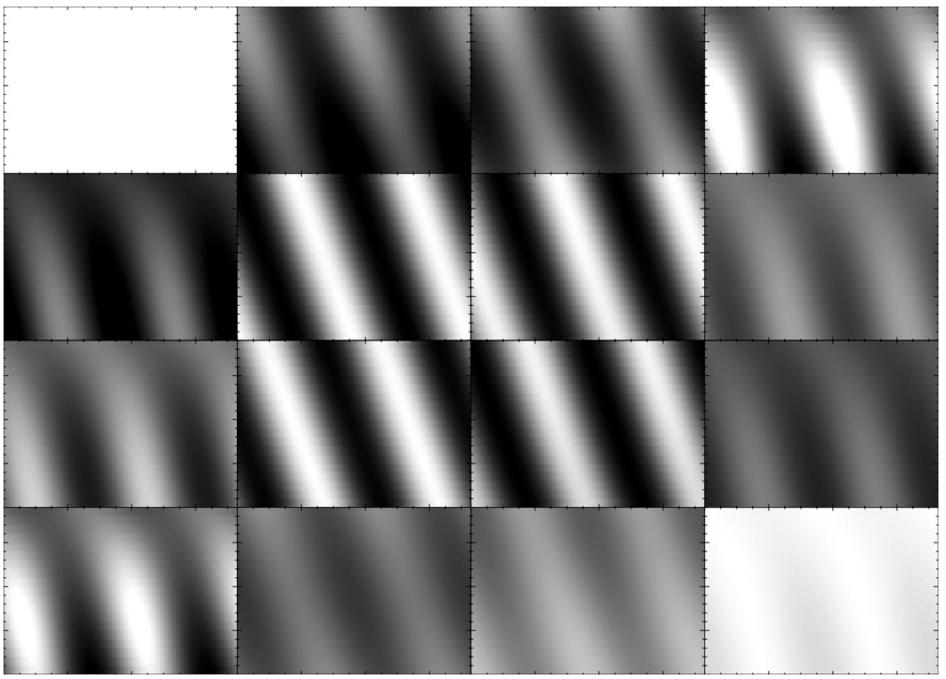

Fig. 17 The Zemax calculated Mueller matrix at the CryoNIRSP modulator for all telescope azimuths and elevations are shown in each panel for zero field at a wavelength of 2500 nm. Each box shows a Mueller matrix element as a function of azimuth (X) and elevation (Y). Azimuth is increasing horizontally on the X-axis from 0 deg at left to 360 deg at right of each element. Elevation is increasing vertically (Y) from the horizon (0 deg) at the bottom to the zenith (90 deg) at the top. Thus, each box shows a Mueller matrix element over the full hemisphere (azimuth from 0 deg to 360 deg and elevation from 0 deg to 90 deg) of possible optical pointings, which is beyond the actual capabilities of the telescope mechanical structure. This clearly shows the simple functional form of the Mueller matrix with azimuth and elevation. Each Mueller matrix element can be represented as sin and cos functions of $2*$ azimuth, elevation, and $2*$ elevation. This is caused by the crossing and uncrossing of the S- and P- planes of the fold mirrors. This is also the same as shown for the AEOS telescope[52] where on-sky calibrations have the same dependence and were easily fit with simple trigonometric functions. The QUV to QUV terms are linearly scaled to amplitudes of ± 1. The intensity to QU terms and the QU to intensity terms (IQ, QI, IU, UI) are scaled to $\pm 1\%$. The IV and VI terms are scaled to $\pm 0.2\%$. For all these I to QUV and QUV to I terms, the $\cos(2\mathrm{Az})$ dependence clearly stands out with an additional dependence on elevation. These terms reach their maximum amplitudes at some (azimuth, elevation) combinations with zero polarization seen only at specific pointings. As the coordinates are fixed with respect to the system entrance pupil for this calculation, there is a strong geometrical rotation seen in the QU to QU terms caused by simple coordinate transformation. However, linear to circular cross-talk is indeed present at some telescope pointings, as seen by the variation in the QV and UV elements. The VV term begins to drop away from 1 at low elevations.

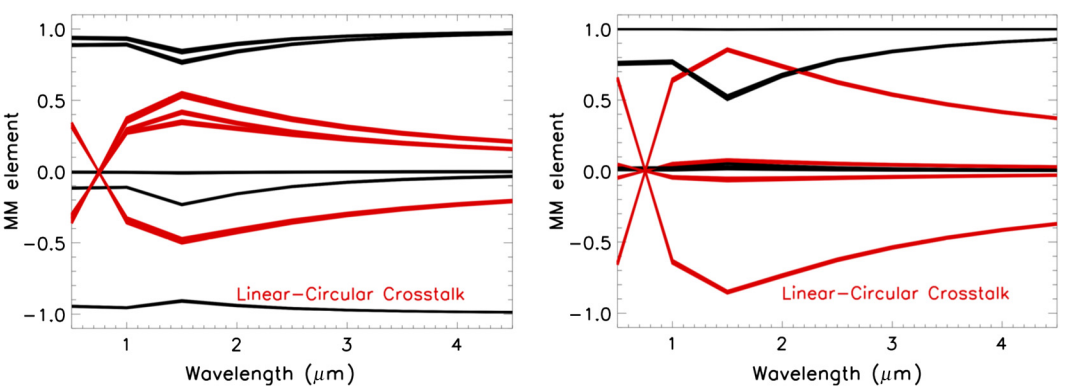

Fig. 18 Mueller matrix elements QUV to QUV for telescope azimuth, elevation combinations of (0 deg, 45 deg) at left and (45 deg, 45 deg) at right. Red lines show the linear to circular cross-talk terms (QUV to QUV). Some cross-talk terms reach amplitudes up to 0.5 at wavelengths around 1500 nm for some pointings. Note that each panel here shows a fixed telescope pointing and represent just a single point in the (Az, El) dependence map of Fig. 17.

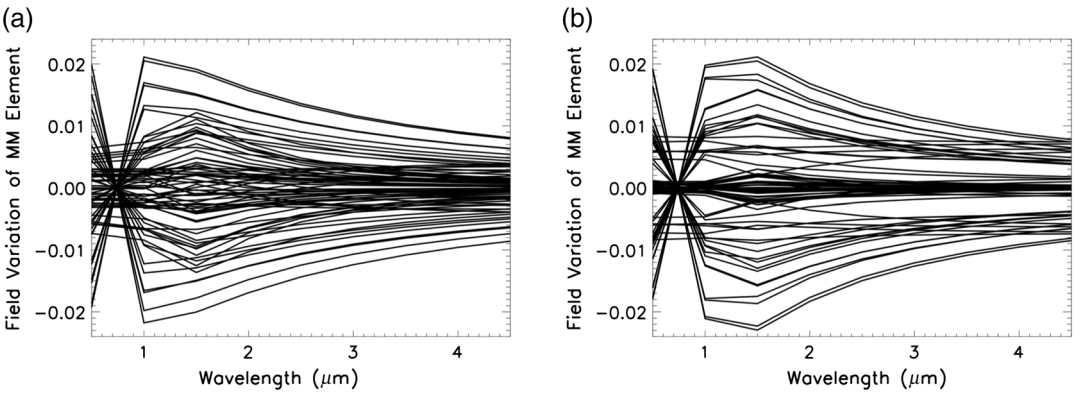

Fig. 19 Mueller matrix element differences between the element at field center and the element at the 5-arc min field edge. Each *QUV* to *QUV* term difference is shown for telescope azimuth, elevation combinations of (0 deg, 45 deg) in (a) and (45 deg, 0 deg) in (b). Different Mueller matrix elements have different field dependencies with wavelength. Some elements have field dependence of up to 0.02 in the value of each element. Note the zero-crossing at 850-nm wavelength of some the lines as roughly the "retardance free" wavelength for the coating formula shown in Fig. 8.

and elevation and leave analysis of the dichric beam splitters to a future paper. We can examine a case where the reflections are enhanced protected silver mirrors and the transmissions are simple uncoated window substrates. We are in the process of modeling formulas and testing dichroic beam splitter coating samples to assess the polarization performance through many layer coatings.

There are a few wavelengths in the visible region where the retardance of the model coating formula matches the witness sample to better than 1 deg. We choose three wavelengths to model the DKIST telescope optics and the ViSP instrument optics to the modulator. At 400-nm wavelength, the model coating formula matches to 0.26 deg. At 600 nm, the retardance matches to 0.80 deg. At 800-nm wavelength, the retardance matches to 0.09 deg. As of this time, ViSP has not yet selected an actual vendor to coat their mirrors so these results are approximate and can easily be rerun once we have more information about the actual coatings chosen by the team.

Figure 21 shows the computed Mueller matrix elements while articulating the telescope Zemax design in azimuth from 0 deg to 360 deg and elevation from 0 deg to 90 deg pointing range, well beyond the actual capabilities of the telescope mechanical structure. As expected, there is a large amplitude QU to QU term variation that represents the geometric rotation between the coordinates of the modulator and the coordinates of the primary mirror in addition to any circular birefringence causing QU to QU polarization effects. As Zemax uses local mirror coordinates, this geometric rotation is present in all models where mirrors are articulated via Zemax coordinate breaks.

As expected, the linear to circular polarization terms are present but are nowhere near as large an amplitude as for the AEOS telescope where we derived similar predictions.[43,52] The DKIST telescope feed optics have a much more benign polarization behavior with azimuth and elevation due to the reduced incidence-angle folds. The AEOS beam has five mirrors at 45-deg incidence angle whereas DKIST has [45 deg, 15 deg, 30 deg, 45 deg]. The AEOS beam has 45-deg incidence before the elevation axis, 135-deg incidence between elevation and azimuth axes, and another 45 deg to level the beam on the coudé floor. For DKIST, these numbers are 45 deg, 45 deg, and 45 deg.

With this coating formula at 400-nm wavelength, the first four mirrors in the DKIST train have a diattenuation less than 5% with (UU, VV) terms of 0.97 and (UV, VU) terms of 0.24. Though the primary and secondary mirrors have substantial incidence angles and variation across the beam, the primary UV term comes from the 45-deg incidence angle of M3. The second group of mirrors is the two flat fold mirrors M5 and M6, which are at incidence angles of 15 deg and 30 deg, respectively. This group of mirrors has essentially the same linear to circular cross talk. The diattenuation is always less than 4% as the telescope is articulated with (UU, VV) terms of 0.96 and (UV, VU) terms of 0.27. This compares quite favorably with a configuration of three separate flat folds working at 45-deg incidence angles articulated in (azimuth, elevation) where the linear to circular terms (UV, VU) can be above 0.85 at certain pointings.[43]

For the remaining ten mirrors on the coudé lab feeding light to the ViSP modulator, the diattenuation is about 4% with (UU, VV) terms of 0.91 and (UV, VU) terms of 0.40. There is a 45-deg incidence angle mirror (M7), two 15-deg incidence angle mirrors (M10, BS2), a powered feed mirror at 28 deg, and four other mirrors below 12 deg.

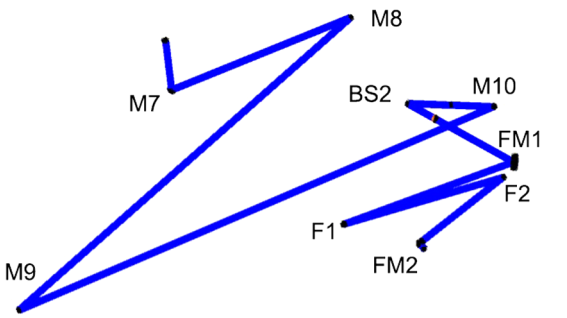

Fig. 20 A schematic layout of the ViSP feed optics on the coudé floor from M7 through the modulator. M7 folds the vertical beam on to the coudé floor at 45-deg incidence angle. The DKIST optics M8–M10 and the beam splitter BS2 feed the ViSP optics. ViSP contains a few feed optics and fold mirrors working at a range of incidence angels. The modulator is immediately after the final fold mirror. This fold is roughly 45-deg incidence angle.

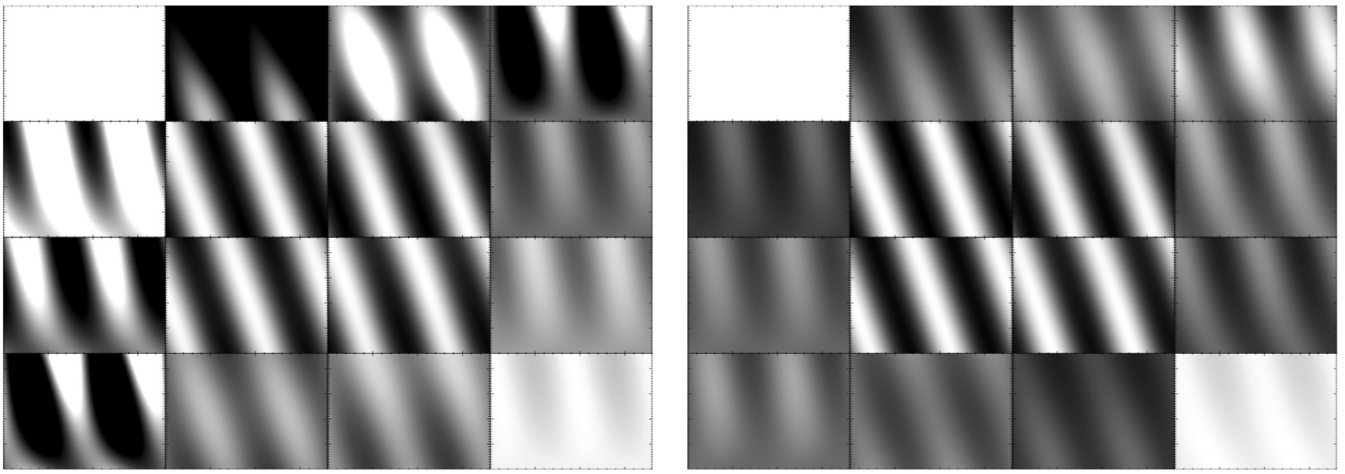

Fig. 21 The Zemax calculated Mueller matrix at the ViSP modulator for all telescope azimuths and elevations are shown in each panel for zero field. The left panel shows a wavelength of 400 nm. The right panel shows a wavelength of 600 nm. Each box shows a Mueller matrix element with azimuth increasing horizontally from 0 deg at left to 360 deg at right and elevation increasing vertically from the horizon (0 deg) at the bottom to the zenith (90 deg) at the top. Each box shows a full hemisphere (azimuth from 0 deg to 360 deg and elevation from 0 deg to 90 deg) pointing range, beyond the actual capabilities of the telescope mechanical structure. The *QUV* to *QUV* terms are linearly scaled to amplitudes of ± 1. The intensity to *QU* terms and the *QU* to intensity terms are scaled to $\pm 4\%$ for the 400-nm model on the left and $\pm 2\%$ for the 600-nm model on the right. The *IV* and *VI* terms are scaled to $\pm 1.0\%$ for the 400-nm model on the left and to $\pm 0.5\%$ for the 600-nm model on the right.

8 Summary

We presented Zemax optical models and performance predictions for the DKIST telescope feed optics and two of the first light polarimetric instruments, the CryoNIRSP and the ViSP. Simple flat fold mirror in a powered beam was studied to demonstrate the sensitivity to Mueller matrix elements to the f/number of the beam. We also explored the limitations inherent in converting the Jones matrices for individual rays to the Stokes vector for the optical model using only the X and Y components of the electric field. The Mueller matrix calculations match the theoretical formula for a flat mirror based on retardance and diattenuation in agreement with theory and previous studies in the literature.

We will be assessing models for grouping the DKIST mirrors together to predict telescope polarization as functions of field, wavelength, and configuration in forthcoming publications. Beam splitter coating models are in progress and typically require 30 to 90 layers. With these coating models, we can assess the performance of the instruments in both reflection and transmission through the beam splitters. Most of the beams fed to the first light instruments interact with the dichroic beam splitter optics 2 to 4 times. In a future work, we will present polarization models of the other DKIST instruments accounting for the many layer dichroic coated optics. Other ray trace programs could potentially be explored in the future. Polaris-M is an in house polarization ray tracing software developed at the University of Arizona Polarization Laboratory.[63–67] The DKIST project has used this to model the polarimetric calibration optics at the Gregorian focus.[53] A forthcoming paper will describe the polarization performance of the calibration optics and polarization fringe predictions.

The Mueller matrix for the Gregorian focus of the DKIST primary and secondary does not have substantial FoV variation at the 10^{-5} amplitudes, agreeing with previous DKIST design studies. The Mueller matrices vary substantially across any individual footprint from a single FoV due to the incidence angle variation across the highly powered primary and secondary mirrors. These variations are substantially reduced when averaging over the footprint of the beam.

A model coating formula for an enhanced protected silver coating was derived to match witness sample data on coating retardance and diattenuation for the DKIST optics. With this model formula, we showed the azimuth–elevation dependence for the system Mueller matrix for CryoNIRSP and ViSP instruments as functions of field and wavelength. The Mueller matrix elements showed 2% variations in the linear to circular polarization terms for CryoNIRSP across a 5-arc min field. We now have a modeling tool that allows us to compute polarization across the FoV as the telescope moves in azimuth and elevation. With these computational tools, we can assess the quality of simple models of grouped mirrors as a way to calibrate the functional dependence of the system Mueller matrix under a wide variety of configurations and variables.

Acknowledgments

This work was supported by the DKIST project. The DKIST is managed by the National Solar Observatory (NSO), which is operated by the Association of Universities for Research in Astronomy, Inc. (AURA) under a cooperative agreement with the National Science Foundation (NSF). We thank Dr. David Elmore for his assistance, guidance, and insight into the long history of work on the DKIST project. We thank Dr. Don Mickey for sharing the ZPL scripts in 2003 as part of early work on the AEOS telescope. This work made use of the Dave Fanning and Markwardt IDL libraries. We also thank a few anonymous vendors for guidance on typical formulas for protected metal coatings. We thank Infinite Optics for witness samples, coating formulas, and assistance from knowledgeable staff.

References

1. J. P. McMulli et al., "Construction status of the Daniel K. Inouye Solar Telescope," *Proc. SPIE* **9145**, 914525 (2014).
2. S. L. Kei et al., "ATST: the largest polarimeter," in *Solar Polarization 6. Proc. of a Conf. held in Maui*, Vol. 437, p. 319 (2011).
3. T. R. Rimmele et al., "Instrumentation for the Advanced Technology Solar Telescope," *Proc. SPIE* **5492**, 944 (2004).
4. J. Marino, E. Carlisle, and D. Schmidt, "Simulation of DKIST solar adaptive optics system," *Proc. SPIE* **9909**, 99097C (2016).
5. J. P. McMullin et al., "Construction status of the Daniel K. Inouye solar telescope," *Proc. SPIE* **9906**, 99061B (2016).
6. L. C. Johnson et al., "Status of the DKIST system for solar adaptive optics," *Proc. SPIE* **9909**, 99090Y (2016).
7. D. F. Elmore, S. R. Sueoka, and R. Casini, "Performance of polarization modulation and calibration optics for the Daniel K. Inouye Solar Telescope," *Proc. SPIE* **9147**, 91470F (2014).
8. D. F. Elmore et al., "The Daniel K. Inouye Solar Telescope first light instruments and critical science plan," *Proc. SPIE* **9147**, 914707 (2014).
9. W. Schmidt et al., "A two-dimensional spectropolarimeter as a first-light instrument for the Daniel K. Inouye Solar Telescope," *Proc. SPIE* **9147**, 91470E (2014).
10. H. Socas-Navarro et al., "High precision polarimetry with the Advanced Technology Solar Telescope," *Solar Phys. Space Weather Instrum.* **5901**, 52 (2005).
11. S. R. Sueoka, R. A. Chipman, and D. F. Elmore, "Characterization of DKIST retarder components with polarization ray tracing," *Proc. SPIE* **9293**, 929308 (2014).
12. W. H. Schubert, E. Petrak, and T. G. Baur, "Measurement of polarization assemblies for the Daniel K. Inouye Solar Telescope," *Proc. SPIE* **9369**, 93690N (2015).
13. A. G. de Wijn et al., "Preliminary design of the visible spectro-polarimeter for the Advanced Technology Solar Telescope," *Proc. SPIE* **8446**, 84466X (2012).
14. A. G. de Wijn et al., "The polychromatic polarization modulator," *Proc. SPIE* **7735**, 77354A (2010).
15. J. Sánchez-Capuchino et al., "Current concept for the 4m European Solar Telescope (EST) optical design," *Proc. SPIE* **7652**, 76520S (2010).
16. F. C. M. Bettonvil et al., "The polarization optics for the European Solar Telescope," in *Solar Polarization 6. Proc. of a Conf. held in Maui*, Vol. 437, p. 329 (2011).
17. F. C. M. Bettonvil et al., "The polarization optics for the European Solar Telescope (EST)," *Proc. SPIE* **7735**, 77356I (2010).
18. M. Collados et al., "European Solar Telescope: project status," *Proc. SPIE* **7733**, 77330H (2010).
19. M. De Juan Ovelar et al., "Instrumental polarisation at the Nasmyth focus of the E-ELT," *Astron. Astrophys.* **562**, A8 (2014).
20. F. Joos et al., "Reduction of polarimetric data using Mueller calculus applied to Nasmyth instruments," *Observatory Oper.* **7016**, 48 (2008).
21. C. U. Keller and F. Snik, "Polarimetry from the ground up," in *Solar Polarization 5: In Honor of Jan Stenflo ASP Conf. Series*, Vol. 405, p. 371 (2009).
22. C. U. Keller et al., "EPOL: the exoplanet polarimeter for EPICS at the E-ELT," *Proc. SPIE* **7735**, 77356G (2010).
23. C. U. Keller, "Solar polarimetry close to the diffraction limit," *Proc. SPIE* **4843**, 100 (2003).
24. M. Rodenhuis et al., "The extreme polarimeter: design, performance, first results and upgrades," *Proc. SPIE* **8446**, 84469I (2012).
25. R. Roelfsema et al., "The ZIMPOL high-contrast imaging polarimeter for SPHERE: design, manufacturing, and testing," *Proc. SPIE* **7735**, 77354B (2010).
26. J. Sánchez Almeida, "Instrumental polarization in the focal plane of telescopes. 2: effects induced by seeing," *Astron. Astrophys.* **292**, 713–721 (1994).
27. J. Sánchez Almeida and V. Martinez Pillet, "Instrumental polarization in the focal plane of telescopes," *Astron. Astrophys.* **260**, 543–555 (1992).
28. J. Sánchez Almeida, V. Martinez Pillet, and A. D. Wittmann, "The instrumental polarization of a Gregory-Coude Telescope," *Solar Phys.* **134**, 1–13 (1991).
29. W. Schmidt et al., "POLIS: a spectropolarimeter for the VTT and for GREGOR," *Astron. Nachrichten* **324**, 300–301 (2003).
30. F. Snik et al., "Design of a full-Stokes polarimeter for VLT/X-shooter," *Proc. SPIE* **8446**, 844625 (2012).
31. F. Snik et al., "SPEX: the spectropolarimeter for planetary exploration," *Proc. SPIE* **7731**, 77311B (2010).
32. F. Snik et al., "The upgrade of HARPS to a full-Stokes high-resolution spectropolarimeter," *Proc. SPIE* **7014**, 70140O (2008).
33. F. Snik, "Calibration strategies for instrumental polarization at the 10-5 level," *Proc. SPIE* **6269**, 62695P (2006).
34. H. Socas-Navarro et al., "Characterization of telescope polarization properties across the visible and near-infrared spectrum. Case study: the Dunn Solar Telescope," *Astron. Astrophys.* **531**, A2 (2011).
35. H. Socas-Navarro, "Polarimetric calibration of large-aperture telescopes. II. Subaperture method," *J. Opt. Soc. Am. A* **22**, 907 (2005).
36. H. Socas-Navarro, "Polarimetric calibration of large-aperture telescopes. I. Beam-expansion method," *J. Opt. Soc. Am. A* **22**, 539 (2005).
37. P. Spano et al., "Optical design of CAOS: a high-resolution spectropolarimeter for the Catania Astrophysical Observatory 0.91-m telescope," *Proc. SPIE* **5492**, 373 (2004).
38. K. G. Strassmeier et al., "PEPSI: the potsdam echelle polarimetric and spectroscopic instrument for the LBT," *Proc. SPIE* **7014**, 70140N (2008).
39. K. G. Strassmeier et al., "PEPSI spectro-polarimeter for the LBT," *Proc. SPIE* **4843**, 4843 (2003).
40. J. Tinbergen, "Accurate optical polarimetry on the nasmyth platform," *Publ. Astron. Soc. Pac.* **119**, 1371–1384 (2007).
41. C. Beck et al., "A polarization model for the German Vacuum Tower Telescope from in situ and laboratory measurements," *Astron. Astrophys.* **443**, 1047–1053 (2005).
42. C. Beck et al., "Polarimetric Littrow Spectrograph—instrument calibration and first measurements," *Astron. Astrophys.* **437**, 1159–1167 (2005).
43. D. Harrington, J. R. Kuhn, and R. Nevin, "Calibrating and stabilizing spectropolarimeters with charge shuffling and daytime sky measurements," *Astron. Astrophys.* **578**, A126–A120 (2015).
44. D. M. Harrington et al., "Achromatizing a liquid-crystal spectropolarimeter: retardance vs. stokes-based calibration of HiVIS," *Publ. Astron. Soc. Pac.* **122**, 420–438 (2010).
45. D. M. Harrington and J. R. Kuhn, "Spectropolarimetric observations of Herbig Ae/Be Stars. I. HiVIS spectropolarimetric calibration and reduction techniques," *Publ. Astron. Soc. Pac.* **120**, 89–117 (2008).
46. D. M. Harrington, J. R. Kuhn, and K. Whitman, "The new HiVIS spectropolarimeter and spectropolarimetric calibration of the AEOS Telescope," *Publ. Astron. Soc. Pac.* **118**, 845–859 (2006).
47. D. Harrington et al., "InnoPOL: an EMCCD imaging polarimeter and 85-element curvature AO system on the 3.6-m AEOS telescope for cost effective polarimetric speckle suppression," *Proc. SPIE* **9147**, 91477C (2014).
48. E. Collett, "Polarized light," in *Fundamentals and Applications*, Vol. **1** (1992).
49. R. A. Chipman, "Handbook of optics," in *Mueller Matrices*, M. Bass, Ed., 14.1–14.15, McGraw Hill, New York (2010).
50. F. Snik and C. U. Keller, "Astronomical polarimetry: polarized views of stars and planets," *Planets* **175** (2013).
51. A. López Ariste and M. Semel, "Eigenpolarimetry: an algebraic approach to polarization-free telescopes and instruments," in *Solar Polarization 6. Proc. of a Conf. held in Maui*, Vol. 437, p. 403 (2011).
52. D. F. Elmore et al., "Utilization of redundant polarized solar spectra to infer the polarization properties of the new generation of large aperture solar telescopes," *Proc. SPIE* **7735**, 77354E (2010).
53. S. Sueoka, "Polarization optical components of the Daniel K. Inouye Solar Telescope," PhD thesis, University of Arizona (2016).
54. D. M. Harrington, J. R. Kuhn, and A. L. Ariste, "Daytime sky polarization calibration limitations,," *J. Astron. Telesc. Instrum. Syst.* **3**(1), 018001 (2017).
55. G. van Harten, F. Snik, and C. U. Keller, "Polarization properties of real aluminum mirrors, I. influence of the aluminum oxide layer," *Publ. Astron. Soc. Pac.* **121**, 377–383 (2009).
56. E. D. Palik, *Handbook of Optical Constants of Solids, Author and Subject Indices for Volumes I, II, and III*, Academic Press, Maryland (1998).
57. Z. Qu et al., "A solar stokes spectrum telescope," *Solar Phys.* **201**, 241–251 (2001).

58. H. D. Noble and R. A. Chipman, "Mueller matrix roots," PhD Thesis, The University of Arizona (2011).
59. H. D. Noble, S. C. McClain, and R. A. Chipman, "Mueller matrix roots depolarization parameters," *Appl. Opt.* **51**, 735 (2012).
60. H. D. Noble and R. A. Chipman, "Mueller matrix roots algorithm and computational considerations," *Opt. Express* **20**, 17 (2012).
61. R. A. Chipman, "Depolarization index and the average degree of polarization," *Appl. Opt.* **44**, 2490–2495 (2005).
62. R. Chipman, "Classification of depolarizing Mueller matrices," in *Frontiers in Optics*, OSA Publishing, Washington, D.C. (2006).
63. G. Yun and R. Chipman, "Three-Dimensional Polarization Ray Tracing, Retardance," in *Int. Optical Design Conf. and Optical Fabrication and Testing (2010), paper IWA6* (2010).
64. W. S. T. Lam et al., "Ray tracing in biaxial materials," *Proc. SPIE* **7652**, 76521R (2010).
65. W. S. T. Lam et al., "Ray tracing in biaxial materials," *Proc. SPIE* **7652**, 76521R (2010).
66. G. Yun, S. C. McClain, and R. A. Chipman, "Three-dimensional polarization ray-tracing calculus II: retardance," *Appl. Opt.* **50**, 2866 (2011).
67. G. Yun, K. Crabtree, and R. A. Chipman, "Three-dimensional polarization ray-tracing calculus I: definition and diattenuation," *Appl. Opt.* **50**, 2855 (2011).

David M. Harrington is the polarimetry scientist at the National Solar Observatory.

Stacey R. Sueoka is the optical systems engineer at the National Solar Observatory DKIST project.